JGR Atmospheres

RESEARCH ARTICLE
10.1029/2018JD029524

Key Points:
- A multispectral algorithm for daytime liquid-top mixed-phase cloud characterization is applied to Himawari-8 AHI
- Subcloud-top phase probing results over the Southern Ocean are compared with spaceborne and shipborne observations
- Global time-resolved observations for mixed-phase clouds with the advanced phase information are enabled from geostationary satellites

Supporting Information:
- Supporting Information S1

Correspondence to:
Y.-J. Noh,
yoo-jeong.noh@colostate.edu

Citation:
Noh, Y.-J., Miller, S. D., Heidinger, A. K., Mace, G. G., Protat, A., & Alexander, S. P. (2019). Satellite-based detection of daytime supercooled liquid-topped mixed-phase clouds over the Southern Ocean using the Advanced Himawari Imager. *Journal of Geophysical Research: Atmospheres*, *124*, 2677–2701. https://doi.org/10.1029/2018JD029524

Received 22 AUG 2018
Accepted 1 FEB 2019
Accepted article online 6 FEB 2019
Published online 4 MAR 2019

Satellite-Based Detection of Daytime Supercooled Liquid-Topped Mixed-Phase Clouds Over the Southern Ocean Using the Advanced Himawari Imager

Yoo-Jeong Noh[1], Steven D. Miller[1], Andrew K. Heidinger[2], Gerald G. Mace[3], Alain Protat[4], and Simon P. Alexander[5,6]

[1]Cooperative Institute for Research in the Atmosphere, Colorado State University, Fort Collins, CO, USA, [2]National Oceanic and Atmospheric Administration, National Environmental Satellite, Data and Information Service, Center for Satellite Applications and Research, Advanced Satellite Products Branch (NOAA/NESDIS/STAR/ASPB), University of Wisconsin, Madison, WI, USA, [3]Department of Atmospheric Sciences, University of Utah, Salt Lake City, UT, USA, [4]Bureau of Meteorology, Melbourne, Victoria, Australia, [5]Australian Antarctic Division, Kingston, Tasmania, Australia, [6]Antarctic Climate and Ecosystem Co-operative Research Centre, University of Tasmania, Hobart, Tasmania, Australia

Abstract Inaccurate mixed-phase cloud parameterizations over the Southern Ocean remain one of the largest sources of disagreement among global models in determining shortwave cloud radiative feedbacks. Suitable global observations supporting model improvements are currently unavailable. The conventional satellite cloud phase retrieval from passive radiometers is strongly biased toward cloud top without further information on the subcloud phase. Mixed-phase clouds with the liquid-top mixed-phase (LTMP) structures are often classified simply as supercooled liquid. This paper presents a daytime multispectral detection algorithm for LTMP clouds, based on differential absorption between liquid and ice in shortwave infrared bands (1.61 and 2.25 μm). The LTMP algorithm, previously developed for polar-orbiting sensors, is applied to Himawari-8 Advanced Himawari Imager (the first of the next-generation geostationary satellites) to probe subcloud phase for mixed-phase clouds over the Southern Ocean. The results are compared with spaceborne active sensor data from CloudSat and CALIPSO. Ship-based field experiment measurements are examined for selected cases to provide a more direct assessment of algorithm performance. The results show that applying the LTMP algorithm to geostationary satellites has potential to provide advanced time-resolved observations for mixed-phase clouds globally with improved sublayer cloud phase information that can support enhancement and validation of global models.

1. Introduction

Clouds play a fundamental role in determining the Earth's global radiation budget and climate sensitivity (Cess et al., 1990; Dufresne & Bony, 2008; Stephens et al., 2012). Many cloud properties, such as cloud cover, phase, temperature, and particle size, play important roles in cloud radiative effects (Liou, 2002). Despite our ability to retrieve these properties, cloud radiative forcing and cloud feedback processes remain one of the main sources of disagreement and uncertainty among global climate models (Caldwell et al., 2016; Vergara-Temprado et al., 2018). The role of low clouds in climate feedback processes, for instance, remains one of the largest sources of uncertainty in the representation of climate change (Bony et al., 2006; Dufresne & Bony, 2008; Vial et al., 2013; Webb et al., 2013; Zelinka et al., 2012, 2013). For a given amount of cloud water, whether the particles are ice crystals or supercooled cloud water droplets results in very different radiative effects (Sun & Shine, 1995). Thus, there is an underpinning need to better understand the interplay between cloud properties and their radiative implications at multiple spatial and temporal scales and particularly in cases of mixed-phase clouds.

Several modeling studies have attempted to reduce the uncertainties tied to cloud radiative feedbacks. Model assumptions controlling the distribution of cloud ice/water phase have significant effects on general circulation model (GCM) predictions of climate sensitivity (Fowler et al., 1996; Li & Le Treut, 1992; Senior & Mitchell, 1993; Winker et al., 2010). The partitioning of ice and liquid (mixed-phase parameterization) is a key source of model uncertainty in cloud impacts to the shortwave radiation profile, and the treatment of mixed-phase cloud processes in GCMs is still highly uncertain, which are described in a

wide assortment of ways (Cesana et al., 2015; Komurcu et al., 2014; McCoy et al., 2014b; McCoy, et al., 2015). A few recent studies have adopted complex cloud physics in model cloud properties in more realistic ways. For instance, Vergara-Temprado et al. (2018) used ice-nucleating particle information with a high-resolution numerical model employing a double-moment microphysics scheme. As they also pointed out, however, such a realistic representation of ice formation processes is challenging in climate models, most of which do not currently simulate the number concentration of ice particles and the associated microphysical processes. Many cloud parameterizations in climate models predict phase change purely as a function of temperature (used to prescribe ice to liquid ratios) as indicated in Kay et al. (2016), but the amount of liquid and ice in real clouds depends on complex interactions between various physical processes beyond temperature alone. They include local feedbacks between cloud droplets, radiation, and turbulence in concert with moisture inversions (occurring often near cloud top), feedbacks dynamically coupled between clouds and the surface, and impacts of concentrations of ice nuclei and cloud condensation nuclei and cloud particle sizes, which are associated with synoptic-scale weather systems (H. Morrison et al., 2012).

When forming cloud particles, numerical models often idealize the vapor deposition process as perfectly efficient in the mixed phase (ice and liquid are well mixed down to the diffusion scale) and use an empirical representation to nucleate ice as a function of temperature (e.g., Gettelman et al., 2010; Meyers et al., 1992). Consequently, a large fraction of supercooled liquid in modeled clouds is converted to ice at temperatures lower than a given threshold, for example, −10 °C. The effects that prescribing mixed-phase clouds in this fashion have on climate predictions are highly uncertain (Lawson & Gettelman, 2014).

In light of these uncertainties, mixed-phase parameterizations must be more carefully examined via observational studies to reduce regional albedo (the ratio of reflected to incoming shortwave radiation at the top of the atmosphere) biases and narrow the uncertainty in cloud feedback and climate sensitivity in the GCMs. Tsushima et al. (2006) emphasize the importance of evaluating the cloud ice distribution by comparison with data for climate sensitivity studies. However, observations of these quantities in mixed-phase clouds are also challenging, and a suitable global observation data set describing the climatology of the vertical profile of cloud phase for model validation is not currently available. Despite some understood limitations (e.g., Alexander & Protat, 2018; Protat, Young, McFarlane, et al., 2014; Protat, Young, Rikus, et al., 2014), the closest observations meeting this need are those of the CloudSat and Cloud-Aerosol Lidar and Infrared Pathfinder Satellite Observation (CALIPSO) active sensors in tandem, which have flown in the NASA A-Train polar-orbiting constellation since 2006 (Stephens et al., 2018). The CloudSat W-band cloud radar (Stephens et al., 2008) provides detailed profiles of cloud hydrometeors at 250-m vertical resolution but cannot distinguish phase and does not detect clouds well below 1- to 1.5-km height (e.g., Protat, Young, McFarlane, et al., 2014). Its sister satellite, CALIPSO (Winker et al., 2009), carries a 532-nm lidar with polarization-enabling phase capability but has difficulty penetrating optically thick clouds to provide this detail throughout cloud depth. Also, these active sensors can only cover very narrow curtain slice areas.

This paper examines a new approach for advancing our knowledge of sublayer cloud phase and adding the dimension of time-resolved observations by applying this technique to next-generation geostationary (GEO) environmental satellites. Our objective is to utilize these new GEO observations to determine the below-cloud-top phase of supercooled liquid-topped clouds, enlisting a novel multispectral algorithm described by Miller et al. (2014). The algorithm, developed on polar-orbiting sensors in anticipation of the future GEO capabilities, makes use of scattered sunlight in narrow shortwave infrared (SIR) bands (1.6 and 2.25 μm) to "probe" below liquid-topped clouds and determine phase based on the differing optical properties of liquid- and ice-phased cloud particles at these wavelengths. Detection is predicated on differential absorption between liquid and ice particles, with this relationship characterized as a function of varying sun/sensor geometry. Compared to the previous cloud phase determinations, the SIR bands provide unique insight on cloud internal structure which the Miller et al. (2014) algorithm (hereafter referred to as the liquid-topped mixed phase, or LTMP, algorithm) attempts to exploit.

The LTMP algorithm has been applied to the Visible/Infrared Imaging Radiometer Suite (VIIRS; Lee et al., 2010) on the Suomi National Polar-orbiting Partnership (S-NPP) and the Joint Polar Satellite System (JPSS) satellites. The SIR bands are also available to the next generation of GEO satellite sensors, including the Himawari-8 Advanced Himawari Imager (AHI; Bessho et al., 2016), the Geostationary Operational Environmental Satellite (GOES)-16 and GOES-17 Advanced Baseline Imager (ABI; Schmit et al., 2017),

and the China Meteorological Administration Feng Yun-4 series (FY-4; the first satellite FY-4 A launched on 11 December 2016; J. Yang et al., 2017) Advanced Geosynchronous Radiation Imager (AGRI). Similar bands will become available on the GEOstationary Korea Multi-Purpose SATellite-2A (GEO-KOMPSAT-2A) Advanced Meteorological Imager (AMI) recently launched on 4 December 2018 and European Organization for the Exploitation of Meteorological Satellites (EUMETSAT) Meteosat Third Generation (MTG; scheduled launch in 2021) with a Flexible Combined Imager (FCI; Just et al., 2014). Based on a global constellation of advanced GEO satellites, more accurate and persistent measurements can be provided, including process studies of cloud phase evolution critical to improving cloud parameterizations.

This paper provides an overview of the LTMP detection algorithm and applications to the Himawari-8/AHI GEO sensor for marine cloud layers over the Southern Ocean. As the first instance of the new-generation GEO imagers, AHI has served as a test bed for applications that can be transitioned to the other GEO members as they come online. The paper is structured as follows: Section 2 motivates the research in the context of significant uncertainties of the clouds of the Southern Ocean. Section 3 introduces satellite data and a cloud property processing system used in this study. The LTMP algorithm is outlined in section 4, and the results from the AHI cases compared against CloudSat/CALIPSO active sensor data are discussed in section 5. As an additional validation method, comparisons against shipborne field program data are presented in section 6 along with the information content of GEO observations, and section 7 concludes the paper.

2. Motivation for Research

2.1. Southern Ocean Cloudiness

The Southern Ocean region (~40–60°S), accounting for approximately 15% of the Earth's surface, is very important to Earth's radiation budget because of its extensive cloud cover and unique pristine maritime air-mass environment (McCoy et al., 2014a). Although modelers have improved cloud parametrizations over the Southern Ocean to better match properties inferred from the limited observations (e.g., Kay et al., 2016), many important climate questions remain. Detailed observational data are critical to understanding the influence of Southern Ocean clouds in shortwave radiative feedbacks and providing more realistic cloud phase descriptions in climate model parameterizations. As such, it is essential to continue examining observational data sets that are capable of detailing cloud phase structure for both improvement and verification of cloud parameterizations.

Recently, environmental satellites have begun to offer unique insight into the structure of clouds over this remote region. Satellite-derived climatologies of cloud cover reveal the fractional cloud cover over the Southern Ocean exceeds 80% (with little seasonality; Bennartz, 2007; Haynes et al., 2011; Mace & Avey, 2017; Mace et al., 2007; A. E. Morrison et al., 2011). Satellite and in situ observations show abundant supercooled liquid in low-level clouds dominant over this region (e.g., Chubb et al., 2013; Hu et al., 2010; Huang et al., 2012; Mace & Protat, 2018a; A. E. Morrison et al., 2011). McCoy et al. (2014a) examined the sensitivity of shortwave reflectance to cloud properties over the Southern Ocean with satellite observations and radiative transfer modeling and found that variations in low cloud fraction may cause changes of reflected solar radiation by 9–11 Wm^{-2}. The radiation effects lead in turn to broad-scale meteorological interactions with the fluxes of heat and moisture at the surface, impacting local and global weather/climate conditions.

2.2. Challenges in Models and Limitations in Satellite Observations

It has long been recognized that large differences in cloud properties exist between satellite-observed and modeled representations for the Southern Ocean. The poor representation of energy fluxes over this region has the potential to severely affect the simulated global energy balance within climate models (A. E. Morrison et al., 2011). Recent studies (Bodas-Salcedo, 2018; Bodas-Salcedo et al., 2014, 2016; Cesana & Chepfer, 2013; Naud et al., 2014; Trenberth & Fasullo, 2010; Zelinka et al., 2013) have indicated the importance of correctly representing the underestimate of cloudiness in these regions which causes significant biases in absorbed sunlight at the ocean surface. Kay et al. (2016) indicated that the modeled clouds (specifically in the Community Atmosphere Model, version 5) have insufficient amounts of supercooled liquid water, and the shortwave radiation biases may be linked to the shallow cumulus parameterization through the thermodynamic phase of these clouds. Vergara-Temprado et al. (2018) suggested that lower ice-

nucleating particle concentrations over the Southern Ocean than in other areas are a major factor in causing a persistent supercooled state in mixed-phase clouds and explaining model biases. Protat et al. (2017) highlighted the inaccurate representation of the cloud-radiation interactions in multilayer Southern Ocean cloud situations in a regional forecast model. McCoy et al. (2016) suggested that excessively converting supercooled water to ice in GCMs tends to induce a more negative cloud radiative feedback in the Southern Hemisphere, which leads to a cooler Southern Ocean, a warmer Tropics, an increased poleward heat transport, and a stronger Southern Hemisphere atmospheric jet. In opposition to the positive global mean cloud-climate feedback for increased greenhouse gases (Boucher et al., 2013), negative cloud feedbacks over the Southern Ocean as inferred by most climate models are a consequence of optical thickness increases resulting from ice-to-liquid cloud phase change (Ceppi et al., 2016; Kay et al., 2014, 2016; Tsushima et al., 2006; Zelinka et al., 2013).

Given uncertainties and errors in global models, it has been desired that satellite observations provide more accurate cloud structure and phase information over this data-sparse region which can support improvement and validation for models. However, existing satellite data sets conventionally from passive radiometers have inherent difficulties in separating ice, water, and mixed-phased clouds (Doutriaux-Boucher & Quaas, 2004; Platnick et al., 2003). Cloud-top phase (which importance has been addressed in modeling studies) is inferred as a function of the brightness temperature difference between the 8.5- and 11-μm channels and the cloud-top temperature (Pavolonis, 2010; Platnick et al., 2003). Nasiri and Kahn (2008) found that 75% of the MODerate-resolution Imaging Spectroradiometer (MODIS) cloudy retrievals between −8 and −23 °C are classified as either mixed phase or uncertain and that multilayer clouds can produce spectral signatures that masquerade as midlevel or mixed-phase clouds. Conventional techniques using the midwave and thermal infrared bands (e.g., Ellrod, 1996; Ellrod & Bailey, 2007; Lee et al., 1997) may classify LTMP clouds simply as either "supercooled liquid" or "mixed." Even stronger absorption by liquid water in the thermal infrared bands (e.g., 8.5-, 10.35-, and 12.3-μm thermal infrared bands of passive radiometers used for cloud-top phase determination; Pavolonis, 2010; Strabala et al., 1994) biases the determination of cloud phase to the uppermost portions of the cloud (~1.0 visible-wavelength optical thickness; Pavolonis et al., 2005), precluding determination of phase properties below cloud top.

2.3. A Simple Radiative Transfer Analysis

Noh et al. (2011, 2013) discuss the general significance of cloud phase information in both radiative transfer and satellite retrievals. To underscore the implications of such structural variation on the extensive low cloud fields of the Southern Ocean, idealized radiative transfer simulations using the Santa Barbara DISORT Atmospheric Radiative Transfer (Ricchiazzi et al., 1998) model were conducted in both the longwave and shortwave parts of the electromagnetic spectrum. These simulations illustrate where and when accurate specification of vertical phase structure impacts the radiation budget of the lower troposphere.

A 3-km-thick cloud was defined between 1 and 4 km with a midlatitude winter atmosphere. The cloud's vertical structure was partitioned according to what has been observed in nature (e.g., field programs such as Fleishauer et al., 2002). Idealized scenarios of "liquid over ice" and "liquid over drizzle" were represented by stacking two homogeneous layers—a top layer of supercooled liquid water residing between 3 and 4 km and a lower layer between 1 and 3 km. The top (liquid) layer was constrained with Effective Particle Size (EPS; also referred to as the effective radius; Hansen & Travis, 1974) of 8 μm, and the lower layer EPS was set to 30 μm for the liquid over ice case and 100 μm for the liquid over drizzle case. In addition, two scenarios of all-liquid and all-ice clouds were included (with EPS of 8 μm throughout), for a total of four distinct cloud configurations.

The results of these simulations are shown in Figure 1. Whereas no significant differences appear in the longwave among the phase profiles, consistent with findings of Zelinka et al. (2012, 2013), significant differences were found in the shortwave. In particular, the liquid over ice (i.e., LTMP) case shows greater heating rates (maximum about 1 K/day) than all-liquid clouds in the lower portions of the cloud and about 1 K/day less than the liquid over drizzle over this same region. Integrated throughout the cloud layer (1–4 km), the total shortwave heating rate was found to be 7.40 K/day for "all liquid," 8.44 K/day for liquid over ice, and 9.42 K/day for liquid over drizzle. Given the widespread coverage and extended lifetime of maritime low clouds in the Southern Ocean (e.g., Haynes et al., 2011), these differences have potential to affect the regional

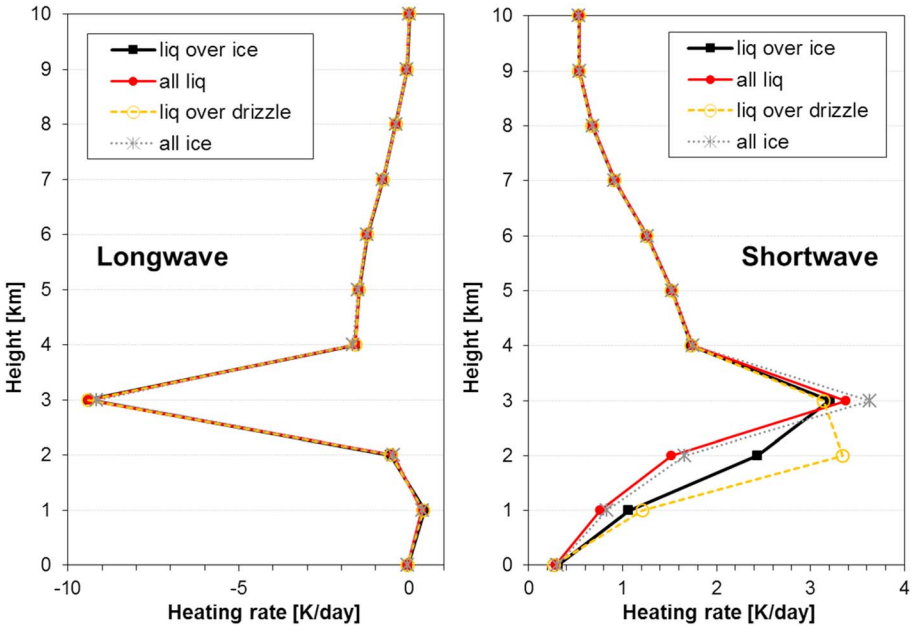

Figure 1. Simulated heating rates for four maritime cloud scenarios (see text for details), showing the sensitivity of shortwave heating rates to assumptions on vertical phase structure.

energy balance, lower tropospheric circulation, and subsequent cloud formation on climatologically relevant scales.

3. Observational Data and Tools

3.1. The Himawari-8 AHI

Himawari-8's AHI (Bessho et al., 2016) is the first of a new-generation of GEO satellites, featuring marked improvements to legacy imaging radiometers in terms of spatial, spectral, temporal, and radiometric resolutions. It offers factors of three, four, and five increases in the spectral, spatial, and temporal resolutions compared to previous sensors available to the geostationary platform. Himawari-8 was launched on 7 October 2014 and settled into a geostationary orbital subpoint of 140.7°E on 16 October 2014.

AHI is a 16-band multispectral radiometer, providing highly advanced spectral imaging capabilities which have been available at the Low-Earth-Orbit (LEO) platform such as MODIS and VIIRS. AHI has three visible bands, three SIR bands, one midinfrared band, and nine thermal-infrared bands, for a total of 16 independent pieces of spectral information. The previous-generation Japan Meteorological Administration geostationary meteorological satellite Multifunctional Transport Satellites (MTSAT) series imager (like those imagers carried on NOAA's previous-generation GOES series ending with GOES-15) had only five spectral bands. AHI obtains multispectral images at high temporal frequencies of 10-min sampling of full-disk imagery and samples at 2.5 min for regional targets. The spatial resolution of the principle visible band and all the infrared bands is about 4 times higher.

The current work uses AHI as a test bed for applying the LTMP cloud detection algorithm (Miller et al., 2014) on GEO for the first time. Developed originally for S-NPP VIIRS, the LTMP algorithm is in principle satellite platform agnostic. For this work, the algorithm was transitioned to AHI to enable study of the temporal evolution of LTMP clouds. The LTMP algorithm will be readily ported to GOES -16/17 and potentially the other next-generation geostationary satellites mentioned above.

Satellite cloud properties derived from AHI, used input to the LTMP detection algorithm, are processed using NOAA's Clouds from Advanced Very High Resolution Radiometer Extended (CLAVR-x) system. CLAVR-x is a NOAA Algorithm Working Group development/transition platform applicable to multiple Low-Earth-Orbit and GEO satellites (Heidinger, 2013; Heidinger et al., 2012). In this study, we apply CLAVR-x to AHI full-disk observations, available at 10-min intervals. A wide range of cloud products are

available from CLAVR-x, including cloud mask, cloud type, cloud top temperature and phase, optical thickness, cloud top particle size, and liquid/ice water path; all provided at AHI's 2-km infrared-band spatial resolution. Since CLAVR-x does not conduct cloud retrievals at boundary pixels of AHI full-disk data (owing to high uncertainties arising from three-dimensional cloud morphology, which violate the plane-parallel assumptions of the retrievals), we consider only areas extending down to 65° S.

3.2. CloudSat and CALIPSO

The results from the LTMP detection algorithm were compared against active remote sensing observations from the CloudSat Cloud Profiling Radar (CPR) and Cloud-Aerosol Lidar with Orthogonal Polarization (CALIOP) onboard the CALIPSO satellite. Whereas a combined lidar/radar observing system would likely outperform any passive radiometer algorithm, these active sensors are available only for a very limited curtain slice through the atmosphere since they are nonscanning sensors and only twice per-day over a region (exact ground track repeat pattern for these sun-synchronous satellites is 16 days). Here we use the active sensor observations as a validation tool, taking advantage of their unique vertically resolving capabilities (Mace et al., 2009; Mace & Zhang, 2014). A brief overview of these active instruments and relevant products follows.

The CloudSat CPR is a near-nadir-looking (0.16° forward) W-band radar (94 GHz; 3-mm wavelength) with a field of view of ~1.3 km in the across-track dimension and ~1.7 km in the along-track dimension. During the time it takes for CloudSat to observe one profile of the atmosphere, the subsatellite point has traveled ~1.1 km along the Earth's surface. This leads to overlap between adjacent profiles. The vertical resolution of CPR range gates is ~480 m, with oversampling increases to ~240 m. Full details of the CloudSat CPR are provided by Stephens et al. (2002, 2008) and Tanelli et al. (2008). In this work, the CloudSat 2B-GEOPROF data product (release version R04; Marchand et al., 2008) was used, which contains radar reflectivity factor and cloud mask. The CloudSat spacecraft began experiencing issues with its main battery in 2011. Since then, the CPR has been configured to operate only during daylight (ascending overpasses), when it can draw additional power from its solar panels.

The CALIPSO CALIOP (Winker et al., 2009) sensor provides direct observations of thin clouds and aerosols from space via two channels 532 and 1,064 nm. Cho et al. (2008) and Hu (2007) investigate techniques for cloud phase determination based on CALIOP depolarization and attenuated backscatter measurements. Owing to strong attenuation of the lidar beam through optically thick media, CALIOP is best suited to the detection of the top boundary of liquid layer clouds (Zhang et al., 2010). In contrast, CloudSat has difficulty detecting the top boundary (due to smaller particles and low water content) but provides the ability to probe down into levels of the cloud where CALIOP cannot, making for a complementary observing system when the two colocated sensors are used in tandem. CALIPSO Validated Stage-1 Level-1B Profile data (the total attenuated backscatter at 532 nm) and Level-2 1-km Cloud Layer data (layer-integrated 532-nm volume depolarization ratio and feature classification flags) were used in this study. The lidar polarization capability is useful for liquid phase discrimination near cloud top. The data also provide temperature values which are obtained from the ancillary meteorological data by the NASA Global Modeling and Assimilation Office Data Assimilation System.

The CloudSat CPR detects various clouds and precipitation but not all clouds in the troposphere. It is sensitive to precipitation-sized hydrometeors but has poor sensitivity to optically thin cirrus (with a small backscatter cross section) and boundary layer clouds due to ground clutter (Mace et al., 2009; Protat, Young, McFarlane, et al., 2014). The shorter wavelength CALIOP lidar can detect much smaller cloud particles and does not suffer from the same surface contamination effects as the CPR but attenuates significantly for deep clouds with visible optical thickness greater than about 3. Mace and Zhang (2014) report global cloud cover is about 76%, while the CloudSat CPR alone estimates ~55%. Boundary layer clouds, dominant below 1 km, are the primary contributor to the missed cloud fractions in the Southern Ocean region. These clouds are easily identified by the lidar. Thus, the complementary CloudSat radar and CALIPSO lidar observations form a powerful observing system for more comprehensive cloud detection and vertical structure information (Forsythe et al., 2012; Miller et al., 2014; Yao et al., 2013).

After the CloudSat battery anomaly in 2011, it became challenging to maintain tight formation with CALIPSO (Nayak et al., 2012). Thus, the official CloudSat-CALIPSO combined products such as 2B-GEOPROF-LIDAR are no longer available since then. However, the two satellites remained in the

A-Train for several years, at a slightly reduced space/time colocation window. The combined information from both sensors was used in this study for evaluation of the LTMP algorithm performance over the Southern Ocean.

3.3. Ship-Based Remote Sensors

A recent field experiment (Clouds, Aerosols, Precipitation, Radiation, and atmospherIc Composition Over the SoutheRN ocean or CAPRICORN) was carried out over the Southern Ocean from 13 March 2016 to 15 April 2016. The experiment featured the Australian Research Vessel (RV) *Investigator* equipped with a suite of modern remote and in situ meteorological instruments. The cloud instrumentation on board the RV *Investigator* included a 95-GHz Cloud Radar called the Bistatic Radar System (BASTA) for Atmospheric Studies with a vertical resolution of 25 m (Delanoë et al., 2016) and a cloud-aerosol Leosphere RMAN-511 mini-Raman lidar operating at 355 nm with a vertical resolution of 15 m. Its main operation area was south of Tasmania, Australia. Most clouds in this region produced radar reflectivity less than −20 dBZ (BASTA radar), and ~30% of the boundary layer cloud cover was observed by the lidar only (consistent with CloudSat/CALIPSO statistics for these clouds). Detailed information and instrumentation deployed for the ship experiment is described by Mace and Protat (2018a, 2018b). Here we utilize the comprehensive remote sensing data series including cloud phase from the combination of the shipborne active sensor measurements during the CAPRICORN voyage for case studies evaluations of the LTMP algorithm applied to AHI. Specifically, we examined two cases on 26 March 2016 and 6 April 2016. Synoptic conditions and ship measurements for those cases are analyzed by Mace and Protat (2018b).

The cloud phase is determined by merging information obtained from the ship-based cloud radar and lidar. The first step is to determine cloud boundaries and phase using the lidar backscatter and depolarization data only, following the procedure outlined by Alexander and Protat (2018). However, we replace their speckle removal algorithm with one that retains clouds based on a threshold value of cloud pixel extent, which we find is effective in removing most noise while qualitatively retaining more real clouds. Ice virga precipitating out of super-cooled liquid water clouds are readily identified by this cloud lidar algorithm—these are flagged as "Ice" in the resultant cloud radar-lidar data product. ERA (ECMWF Re-Analysis)-Interim reanalysis data (Dee et al., 2011) are interpolated around the ship's location to provide vertical profiles of temperature. Liquid and ice cloud phase are determined by considering the relationship between layer-integrated depolarization ratio and backscatter (as in Hu et al., 2010).

The cloud radar is used principally to refine the cloud phase category. The main addition to the classification is a mixed-phase category, which uses the simple rule that when there is no cloud radar signal for lidar pixels classified as "Supercooled-liquid water," the classification remains the same, while if there is a valid cloud radar signal, we reclassify these pixels as "Mixed-phase." The underlying assumption is that the cloud radar does not have sufficient sensitivity to detect supercooled liquid water alone; therefore, the radar detection must be due to large ice particles present in the mixture. The same approach is used in CloudSat-CALIPSO merged cloud phase products (e.g., Delanoë & Hogan, 2010). The second adjustment is when the cloud radar detects a signal at subfreezing temperatures, but the lidar is fully attenuated by lower cloud layers and therefore does not provide any information on cloud phase. In this case, we assign the pixel as a new category, "Mixed-phase or Ice." The category is left nondefinitive since we do not have the information content to separate the two. However, we can at least discern that the phase is not supercooled water or liquid water. CloudSat-CALIPSO products generally classify these pixels as "Unknown."

4. Summary of the LTMP Detection Algorithm

In this section, we briefly summarize a daytime multispectral algorithm proposed by Miller et al. (2014) that attempts to characterize and identify LTMP clouds from passive satellite radiometer. The objective of the algorithm is to identify among a previously identified field of supercooled liquid-topped clouds any that show signs of having an ice-or mixed-phase below cloud top. It does so by utilizing reflected sunlight from SIR bands (1.6 and 2.25 μm); wavelengths that probe to deeper (optical thickness of ~3, for nadir-viewing) levels below cloud top than the 3.9-μm band traditionally used (e.g., Ellrod, 1996; Ellrod & Bailey, 2007; Lee et al., 1997) for daytime cloud top phase analysis. The algorithm is based on differential absorption between liquid and ice particles at these two SIR bands, noting that ice is more absorbing than liquid at 1.6 μm while liquid is more absorbing than ice at 2.25 μm. The differential scattering/absorption behavior becomes more

pronounced with increasing particle size and can be predicted for varying sun/sensor geometry and cloud optical properties, forming the basis for casting the relationship as a simple retrieval algorithm. The requisite SIR bands are available on S-NPP (Joint Polar Satellite System) VIIRS and geostationary satellite sensors such as Himawari-8 AHI, GOES-16 ABI, and other forthcoming international constellation geostationary members listed previously—making the LTMP algorithm potentially useful for global analysis.

By the differential absorption arguments presented in Miller et al. (2014), a LTMP cloud with a subcloud-top ice or mixed-phase layer will produce a different (2.25/1.6 μm) reflectance ratio than what would have been observed for a purely liquid phase cloud. The test has its limitations. The depth of enhanced cloud-top penetration by the two SIR bands depends on the optical thickness of the liquid layer near cloud top and the sun/sensor geometry. The departure of the observed reflectance ratio and idealized all-liquid cloud that shares the same bulk properties (i.e., simulated reflectance based on the same cloud optical thickness [COT], EPS, and sun/sensor geometry as the current observations) is used to gauge the likelihood of the LTMP condition. Considering these assumptions, a conservatively selected, cloud-property-dependent threshold value is used for this determination, as described by Miller et al. (2014). If the difference between the observations and the pure-liquid baseline exceeded this dynamic threshold, then the presence of an LTMP cloud is inferred and reported as a positive detection flag.

To simulate SIR reflectance measurements used for idealized LTMP clouds, radiative transfer calculations for idealized clouds (a simple two-layer cloud model composed of variable fractions of liquid and ice phase) were conducted using the Santa Barbara DISORT Atmospheric Radiative Transfer model for numerous combinations of COT, cloud top EPS, and sun/sensor geometry over 43 million entries. As with most cloud property retrieval schemes, the radiative transfer model used here assumes plane-parallel cloud structure and spherical particles (Mie theory)—an assumption that would be valid for marine boundary layer clouds as considered for this study (see Ricchiazzi et al., 1998). The results of these calculations from look-up tables (LUTs) that are consulted for the current cloud properties and sun/sensor geometry when assessing the LTMP status of a preidentified (by CLAVR-x) supercooled liquid-topped cloud.

The LTMP detection algorithm operates on a pixel-by-pixel basis, following the procedure shown in Figure 2. Please note that solar and sensor geometry information is also used as input. The first determination is whether the pixel has predominately liquid phase at cloud top and cloud top temperatures below 273 K (i.e., supercooled liquid at cloud top). This determination is made via conventional passive-based cloud-top phase methods operationally from the NOAA CLAVR-x Level-2 cloud products. It is noted that any errors/uncertainties in this upstream input will thus be inherited by the LTMP algorithm. In particular, high solar zenith angles (toward twilight) may degrade the accuracy of the input cloud retrievals and the current algorithm performance. The likelihood of a liquid-topped cloud at temperatures >273 K having a subcloud-top mixed phase layer (implying that the cloud resides in a temperature inversion) is deemed very small and thus ignored. In contrast, the potential for a liquid-topped to transition to mixed/ice phase via the Wegener-Bergeron-Findeisen process (Bergeron, 1935) has been observed frequently in nature (Fleishauer et al., 2002; Niu et al., 2008; Shupe et al., 2006, 2008), and thus is the focus of this algorithm.

Using CLAVR-x retrievals of the COT and EPS, a minimum COT (COT_min; required for the LTMP analysis) is selected. For cloud pixels satisfying this threshold, the observed reflectance ratio, RR_OBS, is computed from AHI observations of the two SIR bands as (RR_OBS = R_sat(2.25) / R_sat(1.6)). Using the retrieved COT, cloud-top EPS, and sun/sensor geometry, the precomputed LUTs are consulted to obtain a simulated reflectance ratio (i.e., R_sim(2.25 μm) / R_sim(1.6 μm)) for an all-liquid cloud (RR_SIM_Liquid) assumption. The two spectral ratios are then compared via a final ratio which provides a value that varies about 1.0: (RR_OBS_COMP = RR_OBS / RR_SIM_Liquid). By construction, values of RR_OBS_COMP greater than 1.0 would correspond to LTMP clouds (with increasing confidence as the ratio increases). In practice, when RR_OBS_COMP is found to exceed a specified reflectance ratio threshold, RR_THRESH, the algorithm returns a positive detection for a LTMP cloud at that pixel. Three conservatively chosen RR_THRESH values (1.1, 1.2, and 1.5) are used here which have been obtained as a simple first-order solution, based on analysis of cumulative distribution functions of the liquid-normalized reflectance ratios (RR_SIM_COMP) for all LTMP clouds simulated in the LUT. This process is repeated on the pixel level, until all candidate cloudy pixels in the image have been evaluated.

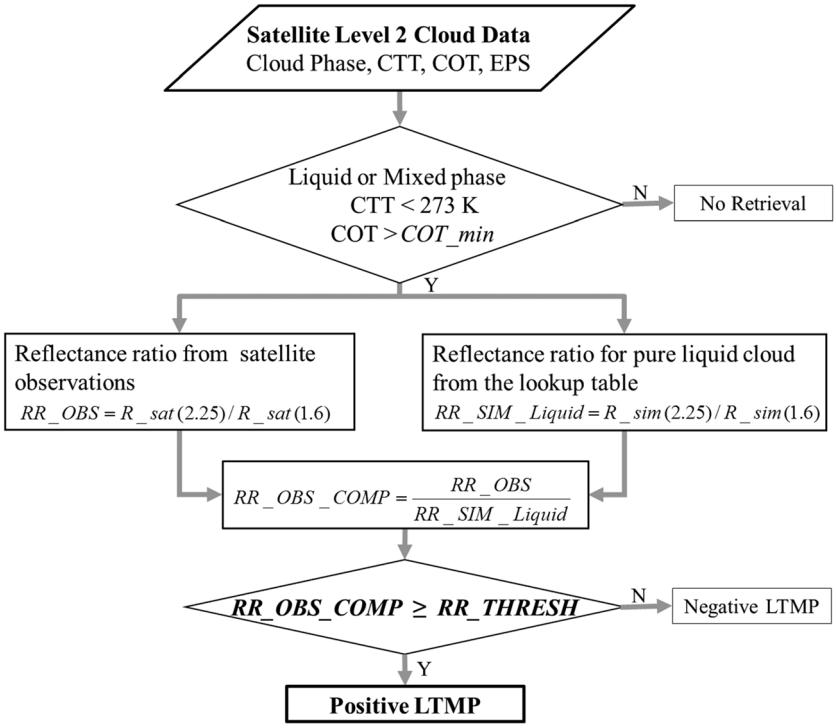

Figure 2. Flow chart of the LTMP cloud detection algorithm (modified from Miller et al., 2014). CTT = cloud top temperature; COT = cloud optical thickness; EPS = effective particle size; LTMP = liquid-top mixed phase.

To build the LUTs, we have used Mie theory for both the liquid and ice layers (spheres). The sublayer cloud heterogeneity may be a complex factor in the current algorithm. To demonstrate that the current algorithm maintains its performance under heterogeneous conditions, we have addressed the subinhomogeneity of drizzle and nonspherical ice particle cases in Miller et al. (2014) and also briefly summarize here. In the previous work, liquid over drizzle idealized cloud scenarios with lower layer particle sizes varying over 30, 50, 100, and 120 μm, while the top particle size was fixed to 12 μm. The radiative transfer model was configured in the same way as the LUT generation runs. The radiative transfer simulations suggest that the presence of drizzle further reduces the observable 2.25-μm/1.61-μm reflectance ratio below values of 1.0 and thus are not a source of ambiguity to the identification of LTMP. In terms of potential impacts to the LTMP algorithm, the misclassification as LTMP for these drizzling clouds was less than 2% when reasonable algorithm thresholds were assumed. It is further noted that the LTMP algorithm cannot determine whether the subcloud-top

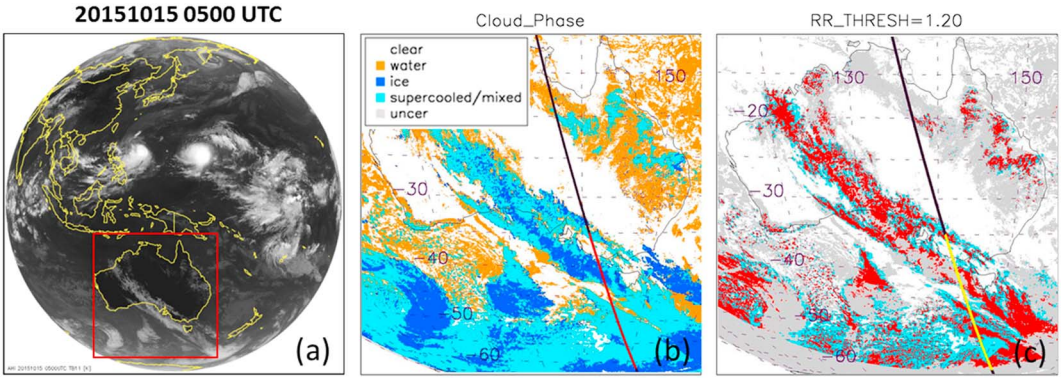

Figure 3. Himawari-8 Advanced Himawari Imager (a) full-disk infrared image at 11 μm, (b) cloud phase from the CLAVR-x system, and (c) liquid-top mixed phase detected pixels (positive liquid-top mixed phase detections in red) based on a threshold value of 1.2 for the 15 October 2015 case (0500 UTC). The black lines in the middle/right panels represent the concurrent CloudSat/ CALIPSO ground tracks (red- or yellow-colored portions of the ground track correspond to profiles shown in Figure 4).

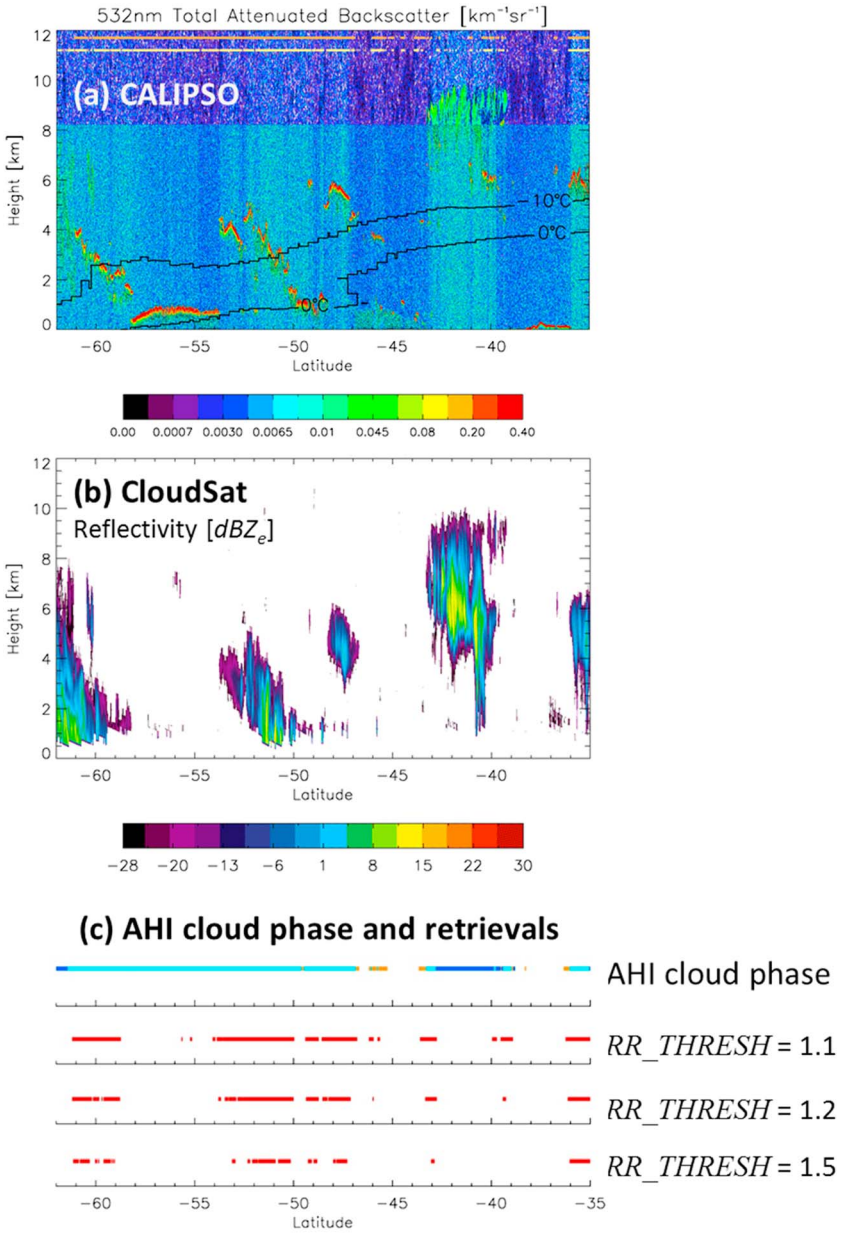

Figure 4. Detection algorithm performance tests with three different thresholds. (a) CALIPSO 532-nm total attenuated backscatter (with the integrated volume depolarization ratio between 0.1–0.3 in light yellow and water phase flags in light orange at the top) and CloudSat (radar reflectivity) observations are shown together, corresponding to the ground track subsets shown in Figure 3. (c) shows cross sections of CLAVR-x-based cloud phase determination, along with the corresponding detection results. AHI = Advanced Himawari Imager.

phase is in a mixed-phase state or fully glaciated phase, although transition to the latter would presumably become more likely in the lower portions (above the melting level) of deeper precipitating LTMP clouds, where the Wegener-Bergeron-Findeisen process has had more time to establish the ice phase.

Spherical particle assumptions in this work may fail to capture the complex single-scatter behaviors of complicated ice morphologies. Tan and Storelvmo (2016) described the phase heterogeneity and associated errors in mixed-phase cloud parameterizations in global models. In Miller et al. (2014), we also conducted sensitivity tests on the spectral single-scatter albedo for sphere and nonspherical ice crystals from P. Yang et al. (2000) and confirmed that the majority of ratios exhibit a similar behavior to the spherical ice

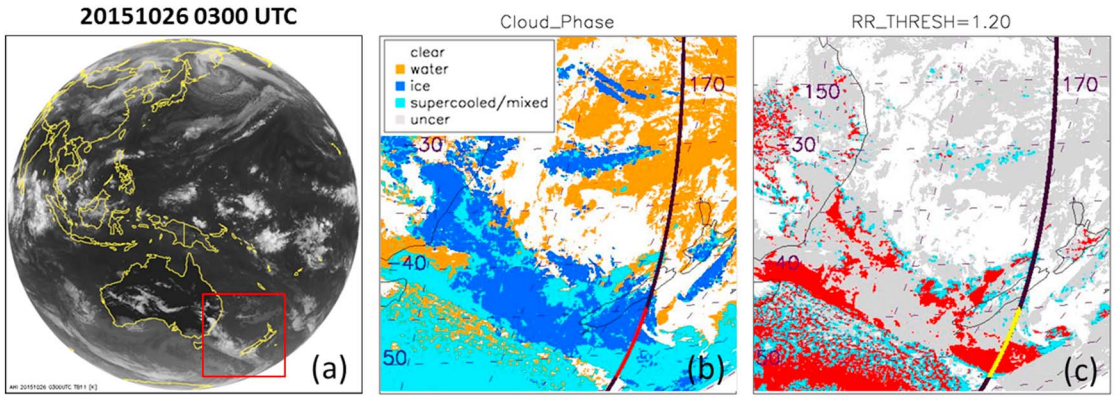

Figure 5. Same as Figure 3 but for the 26 October 2015 case (0300 UTC).

approximation used in this study. Since the sub-ice layer may exist in the LTMP (our target here) is assumed to reside below a semioptically thick (COT > ~1.0) scattering liquid-top layer, the details of the ice scattering phase function may be suppressed, and the global reflectance and transmittance are governed more by the bulk cloud properties. Therefore, we could conclude the current algorithm may perform moderately in those subheterogeneous conditions. Part of the reason for implementing a reflectance ratio, as opposed to simply comparing either the 1.61 or 2.25 μm against a simulated pure liquid cloud signal, was to mitigate such heterogeneity effects. In a summary, our technique is not equipped to make a detailed assessment considering many complicating factors arising from real-world clouds, but the bulk absorption properties offer a chance of at least inferring the presence of the LTMP clouds.

5. Results: Comparisons Against CloudSat/CALIPSO

The LTMP detection algorithm has been applied to S-NPP VIIRS (a LEO platform) for supercooled (or mixed cloud phase) pixels utilizing 1.6 and 2.25 μm to infer the sublayer cloud phase (Miller et al., 2014). It is again noted that the algorithm is applied to only the subset of clouds in the scene that were predetermined to be "supercooled liquid-top" based on conventional passive radiometer phase-determination techniques included within the NOAA CLAVR-x system. In this study, the application of the algorithm was extended to the GEO platform, demonstrated on Himawari-8 AHI.

Since the Japan Meteorological Administration-supplied operational Level-2 AHI cloud products were not yet publicly available at the time of this study, the necessary cloud products used by the LTMP algorithm (cloud mask, cloud phase, cloud top temperature, COT, and EPS) were processed by CLAVR-x using AHI Level-1 full-disk data. As CLAVR-x is a generalized tool, the results shown here for AHI are readily translatable to other members of the next-generation GEO constellation worldwide.

Three cases were considered which offered concurrent CloudSat/CALIPSO overpasses for evaluation of the LTMP algorithm's performance. The target domain for these cases is a portion of the Southern Ocean, south of Australia, and New Zealand where persistent cloud cover has been often observed by AHI. Here accurate cloud phase information would be potentially valuable in determining the correct radiation budget impacts and, by extension, help improve cloud parametrizations in weather/climate models for the Southern Ocean in general.

5.1. Case Study 1: 15 October 2015

The first case study considered a large, ~750-km-wide frontal cloud system extending from the northwestern Australian coast southeastward through Tasmania on 15 October 2015. The expansive cloud deck was composed mostly of midlevel clouds. Figure 3a shows the Himawari-8 AHI full-disk infrared image (for the 11.2 μm "Band 14"), collected at 0500 UTC for this case. A red box drawn on this figure denotes the focus region of the analysis to follow, where CloudSat and CALIPSO provided matching observations for verification of the LTMP algorithm.

Figure 3b shows the CLAVR-x determined cloud phases for this case. Supercooled liquid water (possibly mixed-phase since CLAVR-x currently provides supercooled liquid category only), shown in cyan colors,

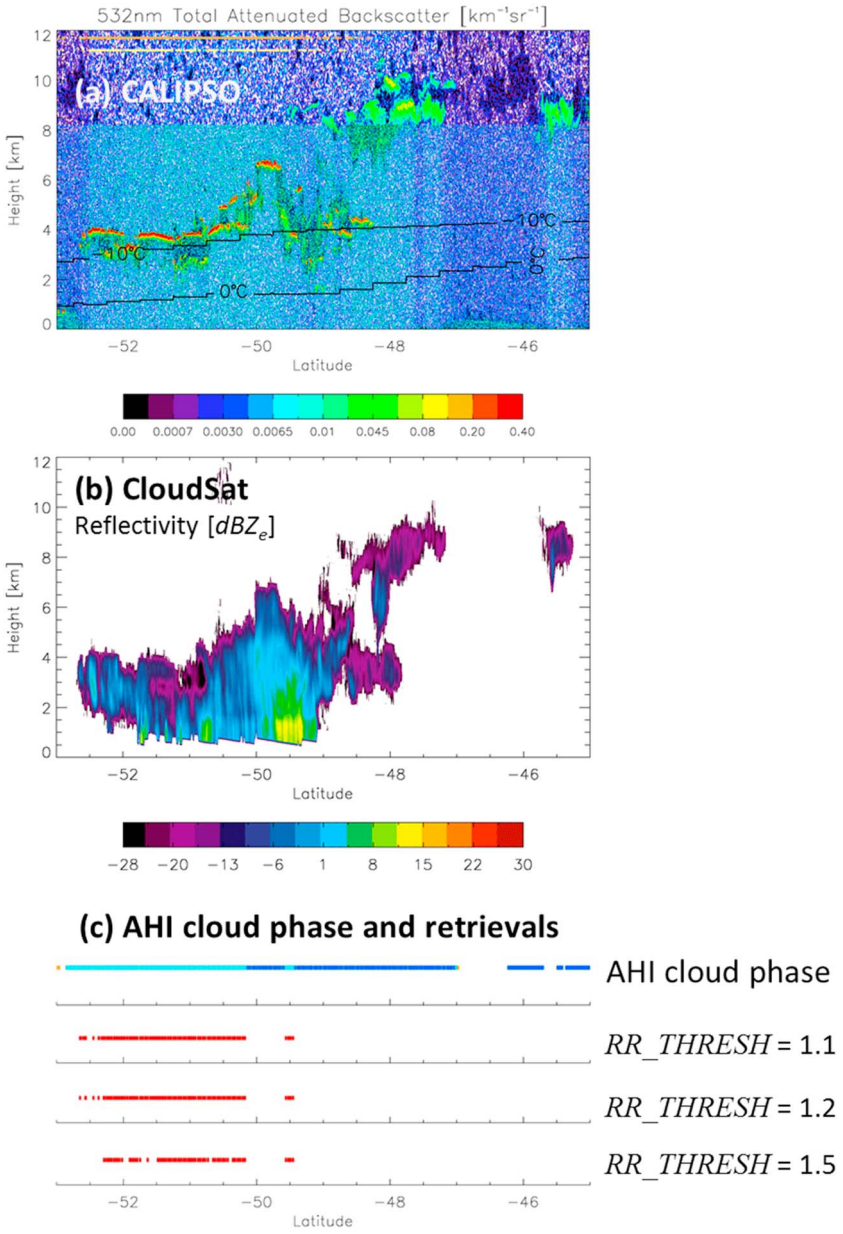

Figure 6. As in Figure 4, but for the 26 October 2015 case (0300 UTC). AHI = Advanced Himawari Imager.

is the dominant cloud top phase classification and is interspersed with ice. As described in section 4, the LTMP algorithm only considers the supercooled liquid top cloud regions. Figure 3c shows as red pixels the subset of those clouds determined as possibly LTMP (positive-detection). Clouds that were not considered by the LTMP algorithm (either due to their temperatures exceeding 273 K or being in the ice phase at cloud top) are represented in gray in the domain. The LTMP detections correspond to a threshold (RR_THRESH) of 1.2; detection results with thresholds of 1.1 and 1.5 are not shown here but are considered in the CloudSat/CALISPO analysis to follow.

The CloudSat/CALIPSO ground tracks for this case are overplotted as black lines, with subsets of these tracks shown in yellow/red colors of Figures 3b and 3c, respectively, corresponding to the exact range of profile extraction for this analysis. These colocated active sensor observations were used in tandem to infer the presence of possible LTMP clouds. The CALIPSO lidar depolarization and backscatter intensity information

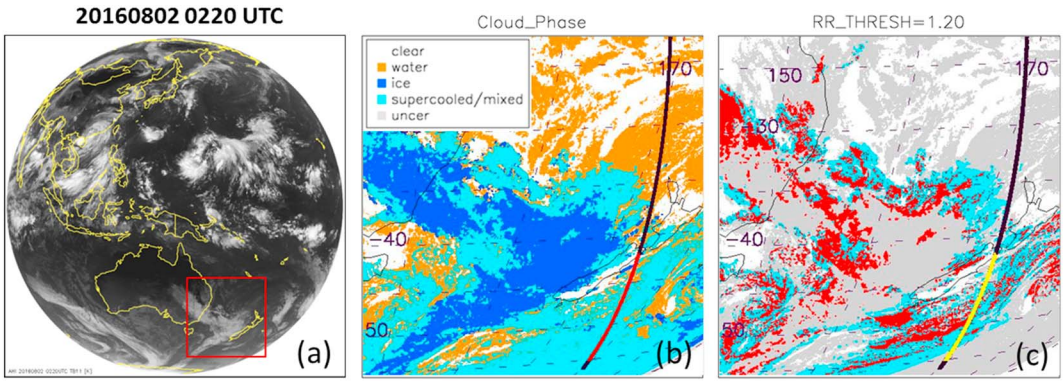

Figure 7. As in Figure 3 but for the 2 August 2016 case (0220 UTC).

(which provides phase discrimination per Hu et al., 2007) indicates the presence of supercooled liquid water at cloud top along the cross-section. In CALIPSO data, ice crystals produce less intense backscatter than mixed-phase clouds (Hu et al., 2007; Lawson & Gettelman, 2014). In contrast, liquid-phase clouds exhibit a strong backscatter followed by sharp gradient due to strong attenuation below cloud top (and often devoid of a surface return). The integrated lidar depolarization ratio for liquid phase is in a range of 0.1–0.3, while the ratio is generally greater than 0.3 for ice phase (Hu et al., 2007). Temperatures from the NASA Global Modeling and Assimilation Office Data Assimilation System (embedded in the CALIPSO data), matched to the observations, are shown as black contours in the CALIPSO backscatter cross sections. CALIPSO-inferred liquid water signatures that reside at altitudes above this numerical model-defined freezing were considered to be supercooled liquid-top clouds. These supercooled liquid signatures were present in much of the CALIPSO data for this case, with the exception of 41–43° S, where 10-km altitude ice-topped clouds were present. These ice clouds were also identified by CLAVR-x and screened-out from consideration by the LTMP algorithm.

The complete attenuation of CALIPSO in liquid-topped clouds limits its ability to describe the full cloud profile. Information below cloud top is revealed by the CloudSat and is used in conjunction with the CALIPSO information to infer the full LTMP morphology. High radar reflectivity (exceeding 8–10 dBZ_e between 50–53° S and 59–61° S) suggests the presence of larger precipitation-sized particles beneath CALIPSO-inferred regions of cloud top supercooled liquid water. However, without the presence of an obvious bright band (a sudden increase in radar reflectivity as ice/snow passing through the melting level transitions into drizzle/rain and appears briefly to the radar as very large and reflective liquid hydrometeors), it is difficult to state definitively the presence of mixed-phase particles for this case.

The cross sections of cloud phase and corresponding LTMP detection results were extracted along the CloudSat/CALIPSO ground track (colored portions) shown in Figure 3. The CALIPSO and CloudSat profiles along these segments are shown in Figures 4a and 4b, respectively. Liquid phase from the Level-2 feature classification flags is also shown at the top of the figure. Corresponding cross sections of the LTMP detection results over the ocean for varying RR_THRESH values of 1.1, 1.2, and 1.5 are shown in Figure 4c. The number of LTMP-flagged pixels decreases as RR_THRESH increases, as is expected for more conservative thresholds. At the most conservative value of RR_THRESH = 1.5, regions of positive detection continue to correspond closely with CloudSat and CALIPSO regions of inferred LTMP structure. Also, important to note is a region of supercooled liquid between 54° and 58° S, where the LTMP algorithm does not produce positive detections (save for a few pixels at the most aggressive RR_THRESH value). Here the CloudSat CPR gives no indication of significant reflectivity below the strongly attenuating CALIPSO-defined liquid cloud top—suggesting that this cloud was more likely to be pristine supercooled liquid throughout its depth.

5.2. Case Study 2: 26 October 2015

The second case study was drawn from the same period (11 days later) and general location. Himawari-8 AHI imagery for this case is shown in Figure 5a, collected on 26 October 2015 at 0300 UTC. The red box drawn on Figure 5a encapsulates a portion of the scene that includes the east coast of Australia and New

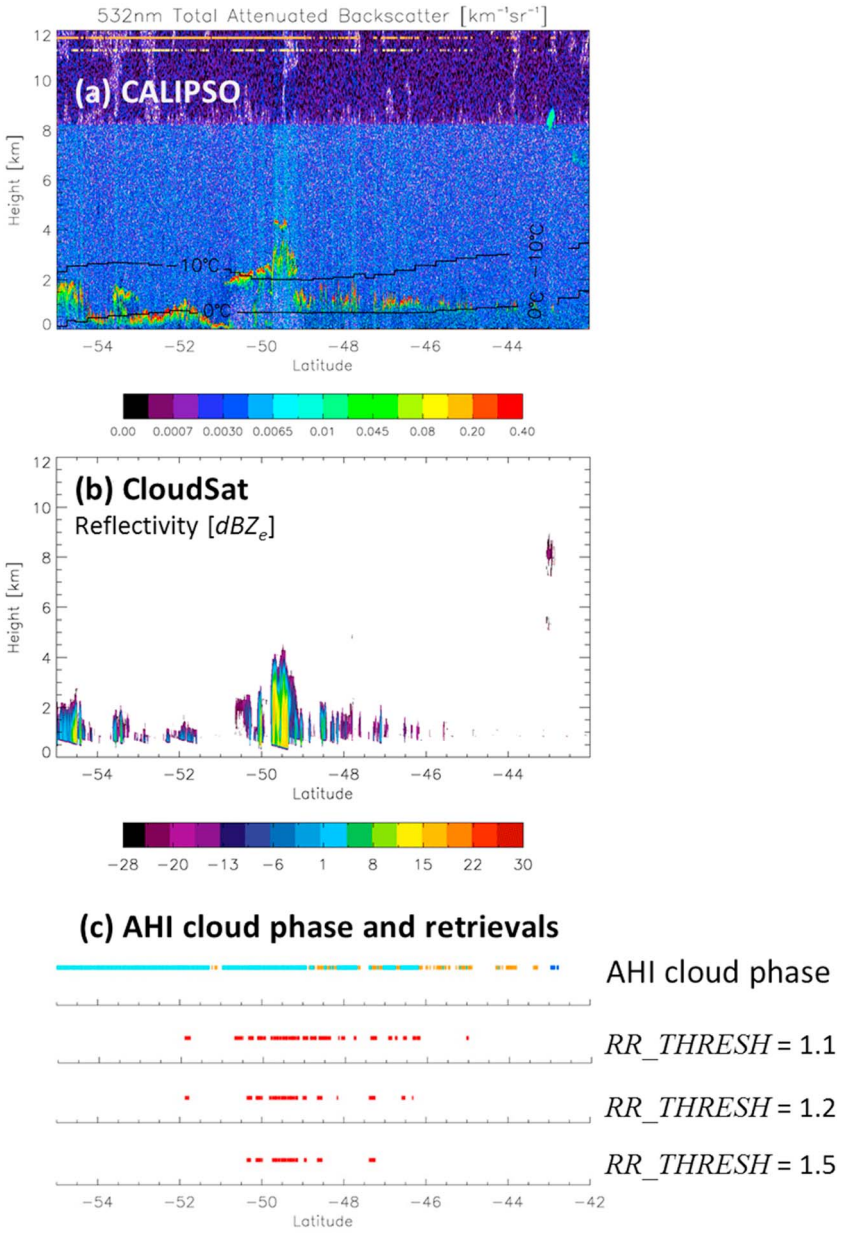

Figure 8. As in Figure 4 but for the 2 August 2016 case (0220 UTC).

Zealand. The imagery in this region shows a broad field of low level to midlevel clouds which, as in the previous case, were associated with a midlatitude frontal system.

Figure 5b shows a mixture of cloud top phase categories over the domain, as identified by CLAVR-x, with the southern clouds dominated by supercooled and ice types. Our focus is on the cloud field south of New Zealand, which includes a CloudSat/CALIPSO overpass. Figure 5c shows the LTMP algorithm results for this region, where again, red pixels correspond to positive detections. The results indicate a region of confident LTMP detection, which then transitions into clouds that were not analyzed by the LTMP algorithm. Inspection of Figure 5b reveals that the exclusion was due to CLAVR-x identification of ice at cloud top (a first-level filter to the LTMP algorithm).

The CALIPSO and CloudSat profiles corresponding to the colored portions of the ground tracks shown in Figures 5b and 5c are shown in Figures 6a and 6b, respectively. Using the same lidar/radar interpretation

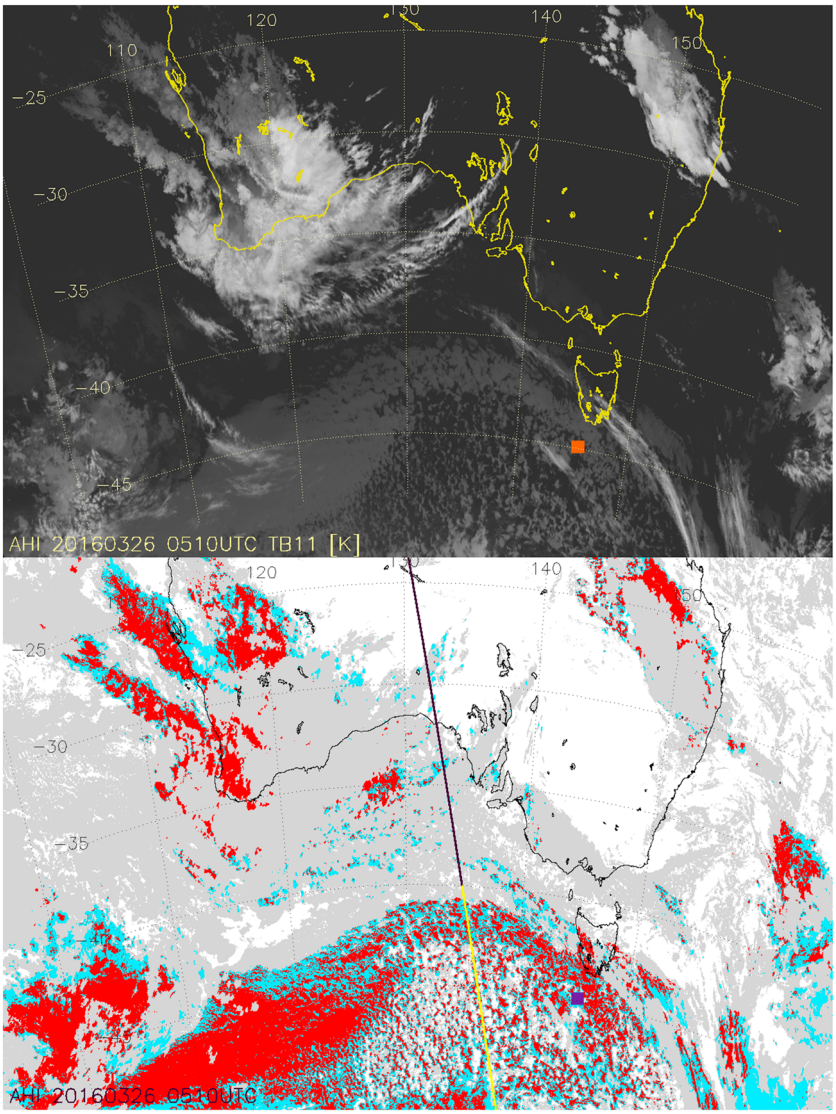

Figure 9. Himawari-8 Advanced Himawari Imager infrared image (11 μm) with the ship location (upper) and liquid-top mixed phase detected pixels (using the threshold value of 1.2; cloud pixels in gray, supercooled cloud phase in cyan, and positive detection in red) with the concurrent CloudSat/CALIPSO ground tracks (bottom) on 26 March 2016 (0510 UTC) during the field campaign. The ship location is indicated with orange or violet symbol.

as in case study 1, we see clear strong evidence for the LTMP structure. In Figure 6b, the CPR data show an obvious bright band structure extending from 49.0° to about 51.75° S (1.6–1.8 km) along the CloudSat ground track, confirming the LTMP structure. At CloudSat/CALIPSO ground track locations northward of about 48.5° S, the cloud deck was observed to change in morphology from midlevel (tops between 4 and 6 km) supercooled liquid to upper-level ice (tops between 8 and 10.5 km). Notice in Figure 6a the marked differences in CALIPSO return strength and attenuation gradient between the supercooled liquid and ice cloud phases. The ice cloud was confirmed by CALIPSO, some portions of CloudSat, and by AHI via CLAVR-x.

Figure 6c shows the LTMP algorithm detections extracted along the CloudSat/CALIPSO active sensor ground track, analyzed for the subset of clouds identified with CLAVR-x as being supercooled. The AHI-based LTMP detections occurred along a latitude range of 49.4–52.3° S. As before, the number of positively identified LTMP pixels decreased when using more conservative thresholds

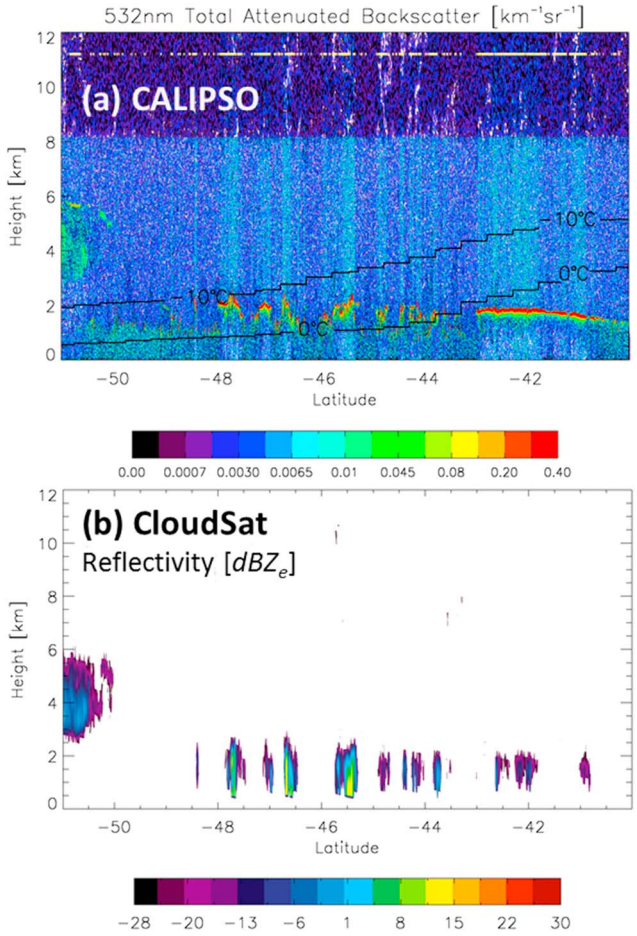

Figure 10. CALIPSO and CloudSat observations along the CloudSat/CALIPSO ground track shown in Figure 9 (yellow segment). (a) Lidar 532-nm attenuated backscatter with the integrated depolarization ratio (0.1–0.3) on the top and (b) radar reflectivity on 26 March 2016 (~510 UTC).

(RR_THRESH = 1.2 and 1.5), but the falloff in this case was not as significant as in the previous case study. The colocated CloudSat and CALIPSO confirmed these cloud structures were indeed LTMP, particularly for the subset of clouds whose tops were below −10 °C (as inferred from the CALIPSO and numerical model matched data). The bright band structures seen in the CPR data and liquid phase signatures at cloud top (high attenuated backscatter plus 0.1–0.3 integrated depolarization ratios) in the CALIPSO data again make a definitive statement on the presence of ice/mixed phase below cloud top, confirming that the LTMP algorithm is performing nominally.

A more complex, mixed array of cloud features existed around 49–50° S, with both ice and supercooled liquid phase cloud tops present. Here CloudSat/CALIPSO data indicated that liquid precipitation was occurring and likely reaching the surface based on the strength of CPR reflectivity in the lowest available range gate (CloudSat profiles are truncated at about 0.75 km above ground level due to ground clutter contamination).

5.3. Case Study 3: 2 August 2016

The final case study analyzed was collected on 2 August 2016, during the austral winter season. Figure 7a shows AHI data from this day, collected at 0220 UTC. Figure 7b (CLAVR-x cloud phase) indicates a large region of frontal clouds, most of which is in the ice phase. However, to the south of New Zealand is a widespread cloud deck whose CLAVR-x defined phase is predominantly supercooled. Among these clouds, only a subset was positively identified by the LTMP algorithm (Figure 7c). The CloudSat and CALIPSO active sensors crossed this region in an ideal location to examine areas of both positive and negative LTMP detection.

Figures 8a and 8b show the cross sections of CALIPSO and CloudSat for this case study, respectively. The active sensor data show that those clouds in general have much lower cloud tops compared to the other two case studies. Throughout the latitudes between 46° and 54° S along the ground track, CALIPSO indicates the presence of supercooled liquid water at cloud top, consistent with the CLAVR-x results. CloudSat shows signals from only a subset of these clouds, corresponding to the larger-sized particles. The LTMP results suggest that the low boundary clouds between 51° and 54° S (1 km or lower) are liquid-phase only, whereas the slightly deeper clouds between 48.5° and 51° S may have a subcloud-top ice/mixed phase. The strongest signal corresponds to the clouds around 49° S, which correspond to the strongest CPR subcloud-top signals as well. While there is no obvious bright band in this case study, the growth of stronger CPR reflectivity suggests the presence of larger particles and the increased likelihood of an established mixed phase in the column. LTMP detections for other low clouds (46–47° S) along the track fall off rapidly when higher RR_THRESH (1.2 and 1.5) values are applied. For these clouds, CloudSat also shows much weaker signals below supercooled liquid cloud top, suggesting a weak/nascent mixed phase or none detected. This case was included mainly for the purpose of illustrating how the LTMP is able to exclude some supercooled cloud fields with skill (i.e., avoiding false alarms for the LTMP structure).

6. CAPRICORN Field Program Comparisons

Although spaceborne active sensors give useful insight to evaluate the LTMP algorithm, validation is still the major challenge due to challenges in ascertaining the phase of the CloudSat-observed fall streaks below the CALIPSO-inferred supercooled cloud top layer. In this regard, CAPRICORN experiment provides valuable data for evaluation to distinguish the subcloud phase and can provide a more direct

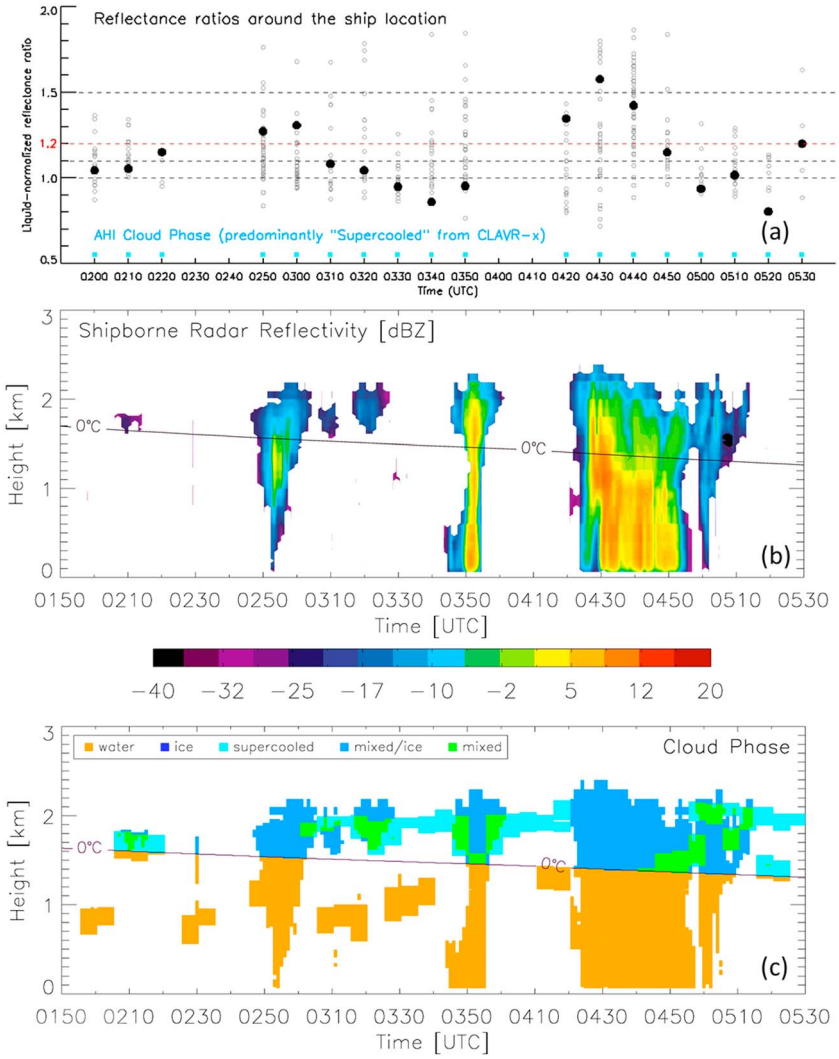

Figure 11. Time series of (a) Himawari-8 AHI reflectance ratios for the liquid-top mixed phase detection together with satellite cloud phase (processed from CLAVR-x) around the ship location (black circles represent mean values and gray dots are individual cloudy pixels within 0.1° distance), (b) 95-GHz shipborne cloud radar reflectivity, and (c) cloud phase from the shipborne lidar-radar and ERA-Interim data with temperature lines during the field campaign on 26 March 2016 (0150–0530 UTC).

assessment of the AHI LTMP algorithm performance. We considered two case studies to conduct this assessment.

6.1. Case Study 1: 26 March 2016

The first case selected was from 26 March 2016, shown in Figures 9 and 10 (with additional AHI movies from 0000 to 0600 UTC as Supporting Information S1). The RV *Investigator* was located southwest of Tasmania, Australia, and sampled various cloud regimes including shallow convections for 24 hr. The shipborne radar and lidar measurements were merged into 25-m spatial and 1-min temporal resolutions. Mace and Protat (2018b) describe this case as a typical cold-air advection scenario, often observed in this region during the CAPRICORN voyage. They note that the majority of clouds were relatively thin nonprecipitating supercooled liquid stratocumulus near the base of the marine inversion, and the lidar depolarization ratios indicated the presence of supercooled liquid for the most part (with temperatures about −7 °C) and occasional ice formation near cloud base on that day.

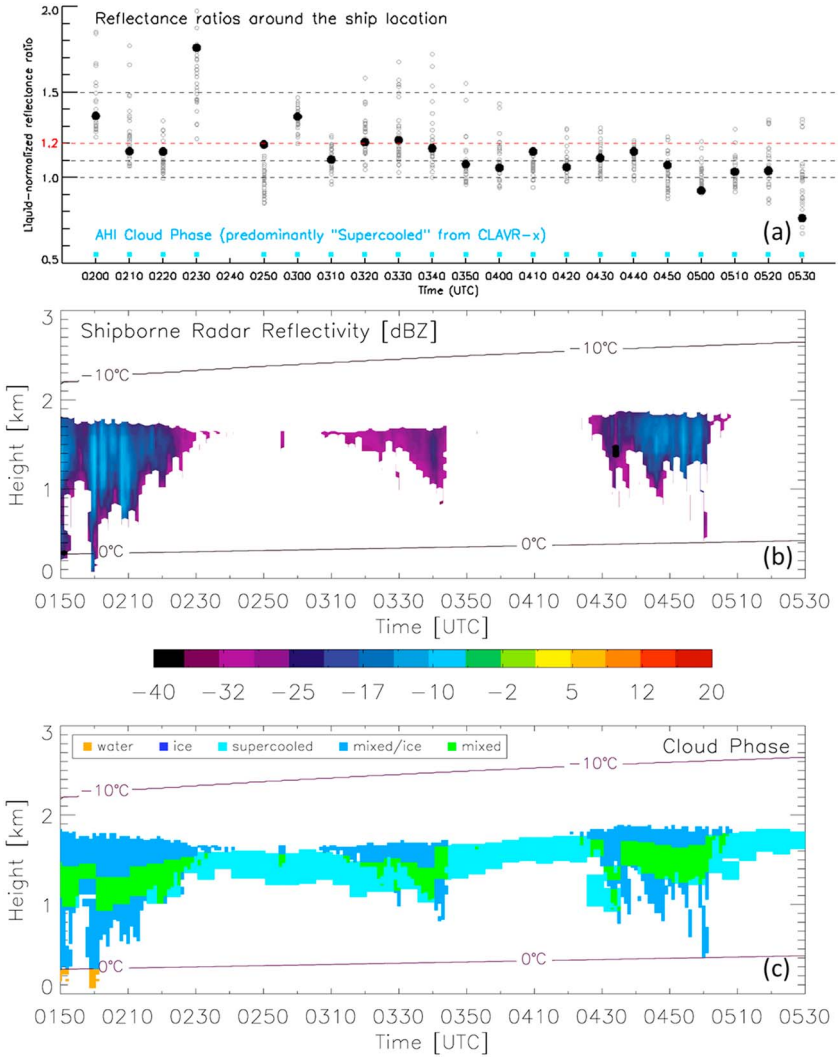

Figure 12. As in Figure 11 but for the 6 April 2016 case.

Figure 9 shows a sample Himawari-8 AHI infrared image (11 μm) with the ship location at 0510 UTC on 26 March 2016. Broad areas of "supercooled" are observed (or possibly mixed in other satellite products since the current CLAVR-x does not provide mixed cloud phase category), and LTMP cloud pixels are widely detected as shown in the figure (using the threshold value of 1.2 in this case). The simultaneous CloudSat/CALIPSO observations confirmed the LTMP structures (Figure 10).

Thanks to the geostationary nature of AHI, consistent and frequent observations were available over this region. Figure 11 shows time series of AHI reflectance ratios for the LTMP detection around the ship location (0200–0530 UTC) on 26 March 2016. Cloudy pixels within 0.1° were averaged. Smaller gray symbols represent the individual pixels in the distance range, and larger black circles depict mean values. Three thresholds for the LTMP determination are shown together in Figure 11, with the 1.2 line emphasized (in red). Cloud top phase as identified by CLAVR-x was predominantly supercooled. For the case, we can see the presence of these long-lived supercooled (or mixed) phase clouds, particularly with LTMP detected pixels. Over the same period, the shipborne 95-GHz Doppler cloud radar reflectivity is shown with a 0 °C temperature line from ERA-Interim reanalysis data in Figure 11b. Cloud phase has been also derived from the shipborne lidar-radar and ERA-Interim data during the experiment (Figure 11c) as described in section 3.3. Compared with the ship observations, the algorithm performed well in detecting the LTMP structured clouds over this region, despite an imperfect spatial matchup.

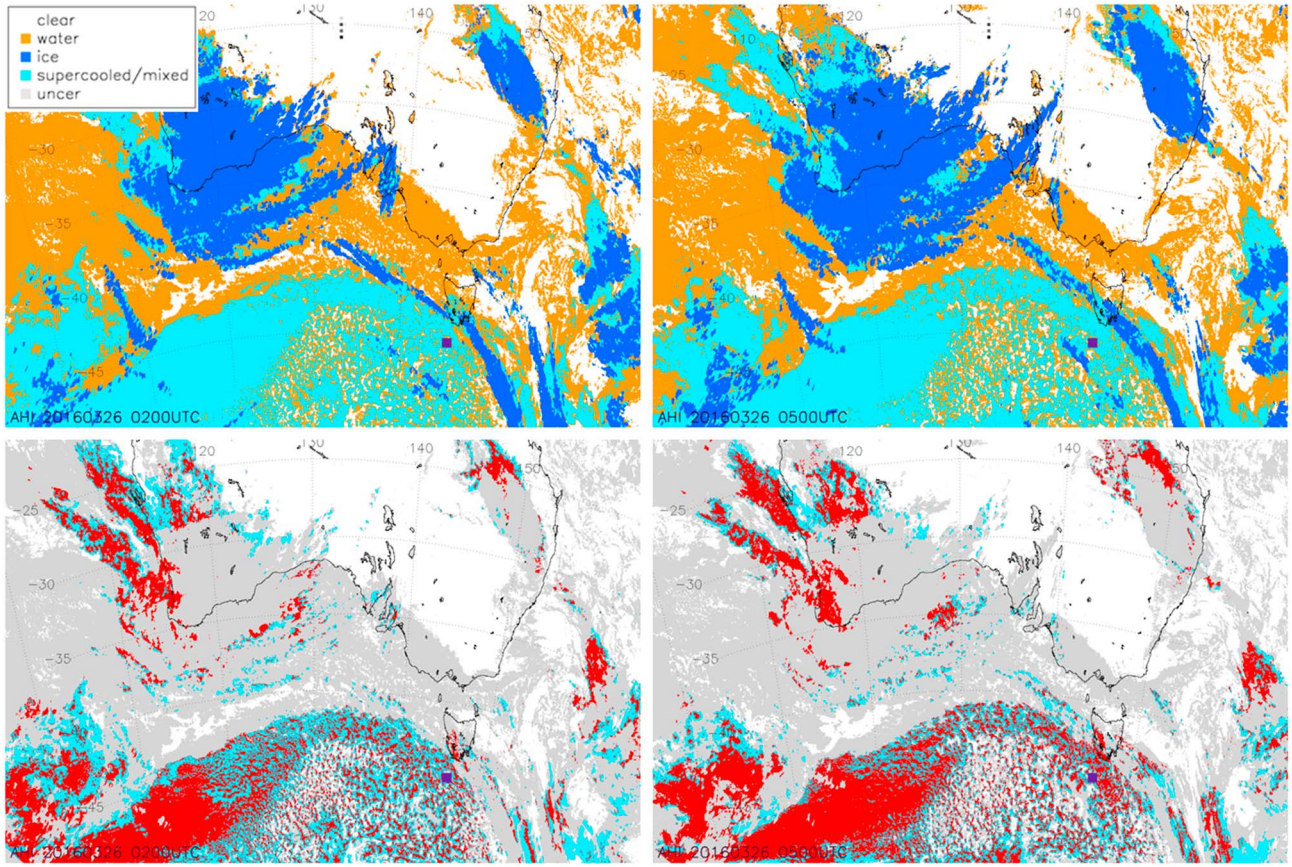

Figure 13. Time evolution of Himawari-8 AHI cloud phase (from the CLAVR-x system) and the liquid-top mixed phase detection (using the threshold value of 1.2) over ocean off the south coast of Australia, selected at 0200 UTC (left) and 0500 UTC (right) on 26 March 2016. The ship location (near Tasmania off the south coast of Australia) is indicated with violet symbols. AHI = Advanced Himawari Imager.

6.2. Case Study 2: 6 April 2016

The second case, from 6 April 2016, is shown in Figure 12. It has been also well described by Mace and Protat (2018b) as being one of the best cases during the ship experiment from the standpoint of highlighting the complementarity of lidar and radar instruments for observing supercooled/mixed phase cloud structures. An extensive layer of supercooled stratocumulus clouds was sampled, and the ship radar/lidar observations showed occasionally drizzling and the presence of the ice phase on that day that rarely reached the surface. Cloud phase from CLAVR-x with AHI again indicates consistent supercooled cloud top over the region. The ship radar and lidar observations are shown together. Please note that the ship cloud phase in the figure, "Mixed-phase or Ice," is flagged when the classification is not definitive but at least can tell it is not supercooled water only (as described previously).

Comparing to the AHI LTMP results, overall, a lower threshold of 1.1 gave a better fit to the detection for this case. When compared with the ship observations, there are a few locations where the LTMP detection algorithm gave false alarms (misidentified as LTMP), particularly for optically thin cloud layers only detected by lidar (e.g., 0230, 0300, and 0410 UTC). However, the results still suggest a potential to reveal the sublayer structures from satellites on a global scale. From the ship observation, it was reported that during the early period between 0200 and 0220 UTC, there was a brief period of ice phase precipitation present scattered in supercooled drizzle, and supercooled liquid drizzle was dominantly observed around 0450–0500 UTC by the radar. These features were well diagnosed by the LTMP algorithm for both periods.

GEO satellite observations provide useful information to track the temporal and spatial evolution of clouds, especially including the LTMP structures. When clouds transition to a mixed-phase state (due to homogeneous freezing of supercooled liquid water droplets or activation of ice condensation nuclei), ice crystals

begin to grow rapidly at the expense of liquid drops (the Wegener-Bergeron-Findeisen process). In the case of a mixed phase cloud forming under conditions with weak or absent vertical motion, it is possible that cloud particles in the mixed phase would evolve rapidly toward ice phase, and the growing ice crystals will descend producing ice virga (or precipitating). Such transition of these clouds can evolve into the LTMP structure over time. We may explore transitions of these clouds related to physical processes, tracking the features with GEO satellite observations.

Persistence of the LTMP structure over 6 hr (daytime observations), as shown in this case study, could be important to assess more accurate radiation budgets over this region. Figure 13 shows samples of cloud phase and LTMP detection (threshold 1.2) at 0200 and 0500 UTC on 26 March 2016, which is at times when daylight was present over the whole domain. The results demonstrate how these LTMP clouds can persist for a significant duration over the Southern Ocean region, and particularly how the sublayer phase evolves into ice phase over time. The latter aspect has not been revealed by conventional cloud-top-only phase products. As briefly discussed in section 2.3, such longer-lived clouds would have a better chance of radiatively influencing the environment via their extended heating/cooling perturbations.

7. Summary and Conclusions

Since the dawn of the space era in the 1960s, satellite-based passive radiometers have been used to determine cloud occurrence. As these measurements have advanced, the ability to glean additional information about cloud morphology, cloud-top phase, and certain cloud macro/microphysical and optical properties has expanded our ability to understand not only cloud occurrence but also cloud processes. These satellite-based remote sensing techniques traditionally have taken advantage of visible, midinfrared, and thermal infrared bands. Cloud phase is often determined via a combination of infrared channels with sensitivity biased strongly toward cloud top. Information concerning phase properties below cloud top from passive observations has proven difficult, even though inverted phase structures (liquid atop ice) are known to be common. The LTMP structure is thought to be particularly frequent in marine boundary layer clouds ubiquitous to the Southern Ocean, as have been observed in nature by many field studies (e.g., Chubb et al., 2013).

To motivate the importance of this study, simple radiative transfer modeling for various cloud structures was conducted, illustrating nonnegligible phase-dependent heating/cooling effects through the vertical extent of the cloud layer. From these simulations, significant heating rate changes were found in the shortwave spectrum. In particular, liquid over ice structures (equivalent to the LTMP in the current algorithm) showed greater heating rates (~1 K/day) than the case with liquid only throughout the vertical layer. When considering the widespread and persistent nature of these midlevel clouds over the Southern Ocean, the results suggest that the subcloud phase determination has the potential to considerably impact the total radiation budget and regional circulation. New observations of cloud phase structure can help to provide GCMs with more complete information for improved parameterizations and forecast skill.

Building on the work of Miller et al. (2014), an algorithm targeting the daytime detection of clouds having liquid-top phase and mixed-phase or pristine ice below cloud top, exploiting SIR bands to determine cloud phase, has been introduced and evaluated on geostationary-based satellite observations for the first time. The LTMP algorithm begins with upstream information about cloud mask, cloud-top-phase, cloud-top particle size, and COT. This information is used to isolate candidate clouds for in-depth analysis using SIR reflective band ratios. Specifically, sunlight in the 1.6- and 2.25-μm SIR bands is used to probe deeper into the cloud (to about an optical thickness of 3), below cloud top, where phase can then be inferred by the ratio of reflectance for these bands. The critical reflectance ratio for denoting the presence of a subcloud-top mixed phase varies as a function of sun/sensor geometry. Originally developed on synthetic (model) data and demonstrated first on S-NPP VIIRS, the algorithm was designed with future GEO satellites in mind, such as Himawari-8/9 AHI and GOES-R ABI. The current work realizes that vision.

The performance with Himawari-8 AHI data has been tested for clouds over the Southern Ocean. Net cloud radiative effects are very sensitive to the representation of mixed-phase clouds and supercooled liquid (Lawson & Gettelman, 2014), and more comprehensive observations are essential over this region. These clouds represent a critical source of shortwave albedo bias and uncertainty within GCMs, and thus a driving key factor in overall uncertainties to the Earth radiation budget which govern the fidelity of climate

predictions. The hope is that the current work can assist with mixed-phase cloud parameterizations, poorly represented in current GCMs, to improve their representation and role in the energy budget of the Southern Ocean.

Three cases over the ocean south of Australia and New Zealand were analyzed for AHI-based LTMP detection, and the results were compared against CloudSat/CALIPSO overpasses. The coupling of lidar, radar, and model temperature profiles provided a useful means of inferring supercooled liquid cloud-top and subcloud top mixed phase, particularly in cases when a bright band exists in the radar profile. The active observations from CloudSat and CALIPSO showed consistent performance of the LTMP algorithm both in terms of positive detections and nondetections. Two additional cases were selected from the CAPRICORN ship-based field experiment which was conducted over the Southern Ocean from 13 March 2016 to 15 April 2016. The results have been compared with the shipborne radar and lidar observations and suggested the LTMP detection algorithm can be applied as a useful tool to reveal the sublayer structures from satellites on a global scale.

With advantages of geostationary orbits, frequent observations on transition and lifetime of these clouds over the Southern Ocean are possible. Our case study analyses using Himawari-8 AHI show that LTMP clouds prolific to the Southern Ocean region are common, and the sublayer phase evolves into ice phase over time. These findings have not been revealed by traditional cloud-top-only phase products. The long-lived nature of these mixed-phase clouds lends to their importance in terms of radiative heating/cooling effects.

The statistical significance of these results has not been investigated yet due to the small sample size. Therefore, a detailed climatology of the LTMP results is a next logical step for this research. A more rigorous validation of the current algorithm under a broader variety of conditions, including in situ observations, would be required to help identify and characterize the performance in a comprehensive way. Such detailed analysis could lead to further improvements, for example, via introduction of addition spectral bands or fused with independent observations. Nonetheless, the current study shows promising results and an important proof-of-concept for applications on the full complement of sensors to join the next generation satellites. The international satellite constellation (such as Himawari-8/9 AHI, GOES-16/17 ABI, GeoKOMPSAT-2A AMI, and MTC FCI) provides global coverage over remote areas, providing key information to form the basis for improved understanding and a source for both improvement and validation of global models.

In future developments, a dynamic threshold based on cumulative distribution functions of reflectance ratios will be explored to provide more robust threshold values for various cloud scenes, although several constant thresholds tested here showed good basic performance. GEO satellite sensors, AHI and ABI matchups with CALIPSO, and/or the future active sensors such as the Earth Cloud Aerosol and Radiation Explorer mission (EarthCARE; Illingworth et al., 2015; launch scheduled for August 2019) will offer more opportunities to obtain robust observational measurement over the Southern Ocean. In a similar sense to our opportunistic usage of CAPRICORN, the algorithm will continue to be evaluated against in situ measurement programs whenever they happen to occur within the satellite's field of view.

The LTMP algorithm was developed on idealized assumptions, and as such, there exist many limitations and areas for algorithm improvement. This daytime technique attempts to infer the LTMP cloud presence via bulk absorption properties, but it cannot make a detailed assessment on what component of the LTMP field is being missed due to lack of sensitivity and cannot be used at night. Some LTMP cloud cases may be missed due to the presence of optically thin cloud layers or due to clouds with subpixel heterogeneity. The applications for multilayered clouds would be very limited due to the nature of this passive measurement technique. As mentioned previously, this algorithm cannot provide a definitive statement on whether the subcloud-top layer is pure ice versus mixed phase. Finally, any errors in the upstream cloud products (from CLAVR-x) used as input to the LTMP algorithm will lead to false detections.

While keeping these important caveats in mind, there remains optimism for taking advantage of the LTMP algorithm when and where it can provide useful information. As with most satellite applications, it represents a “piece of the puzzle” in terms of advancing our overall understanding and view of the complete atmospheric picture.

Acknowledgments
This work was funded by the National Oceanic and Atmospheric Administration (NOAA) GOES-R Program (NA14OAR4320125) and also supported by the Office of Naval Research through Naval Research Laboratory BAA N00173-17-1-G015 and PE-0603207-N. The CloudSat data can be obtained from the CloudSat Data Processing Center (http://www.cloudsat.cira.colostate.edu/), and the CALIPSO data are available through the Atmospheric Science Data Center (ASDC) at NASA Langley Research Center (https://eosweb.larc.nasa.gov/). Himawari-8 AHI data are distributed by the Japan Meteorological Administration for registered National Meteorological and Hydrological Services (NMHSs) users and also sold by Japan Meteorological Business Support Center (http://www.jma-net.go.jp/msc/en/). The CLAVR-x system can be obtained from the NOAA STAR Center for Satellite Applications and Research (http://cimss.ssec.wisc.edu/clavrx/) as part of the Community Satellite Processing Package (CSP). The CAPRICORN field experiment data are available upon request to Alain Protat (alain.protat@bom.gov.au) or publicly available from the CSIRO Data Access Portal (https://data.csiro.au/dap/). The information for radiative transfer model simulations in this paper is properly cited and referred to in the reference list. The views, opinions, and findings contained in this article are those of the authors and should not be construed as an official NOAA or U.S. Government position, policy, or decision.

References

Alexander, S. P., & Protat, A. (2018). Cloud properties observed from the surface and by satellite at the northern edge of the Southern Ocean. *Journal of Geophysical Research: Atmospheres*, *123*, 443–456. https://doi.org/10.1002/2017JD026552

Bennartz, R. (2007). Global assessment of marine boundary layer cloud droplet number concentration from satellite. *Journal of Geophysical Research*, *112*, D02201. https://doi.org/10.1029/2006JD007547

Bergeron, T. (1935). On the physics of clouds and precipitation. In *Proces Verbaux de l'Association de Météorologie* (pp. 156–178). Lisbon, Portugal: International Union of Geodesy and Geophysics.

Bessho, K., Date, K., Hayashi, M., Ikeda, A., Imai, T., Inoue, H., et al. (2016). An introduction to Himawari-8/9—Japan's new-generation geostationary meteorological satellites. *Journal of the Meteorological Society of Japan*, *94*(2), 151–183. https://doi.org/10.2151/jmsj.2016-009

Bodas-Salcedo, A. (2018). Cloud condensate and radiative feedbacks at midlatitudes in an aquaplanet. *Geophysical Research Letters*, *45*, 3635–3643. https://doi.org/10.1002/2018GL077217

Bodas-Salcedo, A., Hill, P. G., Furtado, K., Williams, K. D., Field, P. R., Manners, J. C., et al. (2016). Large contribution of supercooled liquid clouds to the solar radiation budget of the Southern Ocean. *Journal of Climate*, *29*(11), 4213–4228. https://doi.org/10.1175/JCLI-D-15-0564.1

Bodas-Salcedo, A., Williams, K. D., Ringer, M. A., Beau, I., Cole, J., Dufresne, J.-L., et al. (2014). Origins of the solar radiation biases over the Southern Ocean in CFMIP2 models. *Journal of Climate*, *27*(1), 41–56. https://doi.org/10.1175/JCLI-D-13-00169.1

Bony, S., Colman, R., Kattsov, V. M., Allan, R. P., Bretherton, C. S., Dufresne, J. L., et al. (2006). How well do we understand and evaluate climate change feedback processes? *Journal of Climate*, *19*(15), 3445–3482. https://doi.org/10.1175/JCLI3819.1

Boucher, O., Randall, D., Artaxo, P., Bretherton, C., Feingold, G., Forster, P., et al. (2013). Clouds and Aerosols. In T. F. Stocker, D. Qin, G.-K. Plattner, M. Tignor, S. K. Allen, J. Boschung, et al. (Eds.), *Climate Change 2013: The Physical Science Basis. Contribution of Working Group I to the Fifth Assessment Report of the Intergovernmental Panel on Climate Change* (pp. 571–658). Cambridge, UK: Cambridge University Press. Retrieved from http://www.climatechange2013.org/images/report/WG1AR5_Chapter07_FINAL.pdf

Caldwell, P. M., Zelinka, M. D., Taylor, K. E., & Marvel, K. (2016). Quantifying the sources of intermodel spread in equilibrium climate sensitivity. *Journal of Climate*, *29*(2), 513–524. https://doi.org/10.1175/JCLI-D-15-0352.1

Ceppi, P., McCoy, D. T., & Hartmann, D. L. (2016). Observational evidence for a negative shortwave cloud feedback in middle to high latitudes. *Geophysical Research Letters*, *43*, 1331–1339. https://doi.org/10.1002/2015GL067499

Cesana, G., & Chepfer, H. (2013). Evaluation of the cloud thermodynamic phase in a climate model using CALIPSOGOCCP. *Journal of Geophysical Research: Atmospheres*, *118*, 7922–7937. https://doi.org/10.1002/jgrd.50376

Cesana, G., Waliser, D. E., Jiang, X., & Li, J.-L. F. (2015). Multimodel evaluation of cloud phase transition using satellite and reanalysis data. *Journal of Geophysical Research: Atmospheres*, *120*, 7871–7892. https://doi.org/10.1002/2014JD022932

Cess, R. D., Potter, G. L., Blanchet, J. P., Boer, G. J., del Genio, A. D., Déqué, M., et al. (1990). Intercomparison and interpretation of climate feedback processes in 19 atmospheric general circulation models. *Journal of Geophysical Research*, *95*(D10), 16,601–16,615. https://doi.org/10.1029/JD095iD10p16601

Cho, H. M., Yang, P., Kattawar, G. W., Nasiri, S. L., Hu, Y., Minnis, P., et al. (2008). Depolarization ratio and attenuated backscatter for nine cloud types: Analyses based on collocated CALIPSO LIDAR and MODIS measurements. *Optics Express*, *16*(6), 3931–3948. https://doi.org/10.1364/OE.16.003931

Chubb, T. H., Jensen, J. B., Siems, S. T., & Manton, M. J. (2013). In situ observations of supercooled liquid clouds over the Southern Ocean during the HIAPER pole-to-pole observation campaigns. *Geophysical Research Letters*, *40*, 5280–5285. https://doi.org/10.1002/grl.50986

Dee, D. P., Uppala, S. M., Simmons, A. J., Berrisford, P., Poli, P., Kobayashi, S., et al. (2011). The ERA-Interim reanalysis: Configuration and performance of the data assimilation system. *Quarterly Journal of the Royal Meteorological Society*, *137*(656), 553–597. https://doi.org/10.1002/qj.828

Delanoë, J., & Hogan, R. J. (2010). Combined CloudSat-CALIPSO-MODIS retrievals of the properties of ice clouds. *Journal of Geophysical Research*, *115*, D00H29. https://doi.org/10.1029/2009JD012346

Delanoë, J., Protat, A., Vinson, J.-P., Brett, W., Caudoux, C., Bertrand, F., et al. (2016). BASTA, a 95 GHz FMCW Doppler radar for cloud and fog studies. *Journal of Atmospheric and Oceanic Technology*, *33*(5), 1023–1038. https://doi.org/10.1175/JTECH-D-15-0104.1

Doutriaux-Boucher, M., & Quaas, J. (2004). Evaluation of cloud thermodynamic phase parametrizations in the LMDZ GCM by using POLDER satellite data. *Geophysical Research Letters*, *31*, L06126. https://doi.org/10.1029/2003GL019095

Dufresne, J. L., & Bony, S. (2008). An assessment of the primary sources of spread of global warming estimates from coupled atmosphere-ocean models. *Journal of Climate*, *21*(19), 5135–5144. https://doi.org/10.1175/2008JCLI2239.1

Ellrod, G. P. (1996). The use of GOES-8 multispectral imagery for the detection of aircraft icing regions. Preprints, Eighth Conf. Satellite Meteorology and Oceanography, Atlanta, GA, Amer. Meteor. Soc., 168–171.

Ellrod, G. P., & Bailey, A. A. (2007). Assessment of aircraft icing potential and maximum icing altitude from geostationary meteorological satellite data. *Weather and Forecasting*, *22*(1), 160–174. https://doi.org/10.1175/WAF984.1

Fleishauer, R. P., Larson, V. E., & Vonder Haar, T. H. (2002). Observed microphysical structure of mid-level, mixed-phase clouds. *Journal of the Atmospheric Sciences*, *59*(11), 1779–1804. https://doi.org/10.1175/1520-0469(2002)059<1779:OMSOMM>2.0.CO;2

Forsythe, J. M., Dodson, J. B., Partain, P. T., Kidder, S. Q., & Vonder Haar, T. H. (2012). How total precipitable water vapor anomalies relate to cloud vertical structure. *Journal of Hydrometeorology*, *13*(2), 709–721. https://doi.org/10.1175/JHM-D-11-049.1

Fowler, L. D., Randall, D. A., & Rutledge, S. A. (1996). Liquid and ice cloud microphysics in the CSU general circulation model. Part I: model description and simulated microphysical processes. *Journal of Climate*, *9*, 489–529.

Gettelman, A., Liu, X., Ghan, S. J., Morrison, H., Park, S., Conley, A. J., et al. (2010). Global simulations of ice nucleation and ice supersaturation with an improved cloud scheme in the Community Atmosphere Model. *Journal of Geophysical Research*, *115*, D18216. https://doi.org/10.1029/2009JD013797

Hansen, J. E., & Travis, L. D. (1974). Light scattering in planetary atmospheres. *Space Science Reviews*, *16*(4), 527–610. https://doi.org/10.1007/BF00168069

Haynes, J. M., Jakob, C., Rossow, W. B., Tselioudis, G., & Brown, J. (2011). Major characteristics of Southern Ocean cloud regimes and their effects on the energy budget. *Journal of Climate*, *24*(19), 5061–5080. https://doi.org/10.1175/2011JCLI4052.1

Heidinger, A., Evan, A. T., Foster, M. J., & Walther, A. (2012). A naive Bayesian cloud-detection scheme derived from CALIPSO and applied within PATMOS-x. *Journal of Applied Meteorology and Climatology*, *51*(6), 1129–1144. https://doi.org/10.1175/JAMC-D-11-02.1

Heidinger, A. K. (2013). ABI cloud height algorithm theoretical basis document (ATBD). NOAA NESDIS Center for Satellite Applications and Research (STAR), Ver. 3.0, released 06/11/2013. Retrieved from http://www.star.nesdis.noaa.gov/goesr/docs/ATBD/Cloud_Height.pdf

Hu, Y. (2007). Depolarization ratio-effective lidar ratio relation: Theoretical basis for space lidar cloud phase discrimination. *Geophysical Research Letters*, *34*, L11812. https://doi.org/10.1029/2007GL029584

Hu, Y., Rodier, S., Xu, K., Sun, W., Huang, J., Lin, B., et al. (2010). Occurrence, liquid water content, and fraction of supercooled water clouds from combined CALIOP/IIR/MODIS measurements. *Journal of Geophysical Research*, *115*, D00H34. https://doi.org/10.1029/2009JD012384

Hu, Y., Vaughan, M., Liu, Z., Lin, B., Yang, P., Flittner, D., et al. (2007). The depolarization–attenuated backscatter relation: CALIPSO lidar measurements vs. theory. *Optics Express*, *15*(9), 5327–5332. https://doi.org/10.1364/OE.15.005327

Huang, Y., Siems, S. T., Manton, M. J., Hande, L. B., & Haynes, J. M. (2012). The structure of low-altitude clouds over the Southern Ocean as seen by CloudSat. *Journal of Climate*, *25*(7), 2535–2546. https://doi.org/10.1175/JCLI-D-11-00131.1

Illingworth, A. J., Barker, H. W., Beljaars, A., Ceccaldi, M., Chepfer, H., Clerbaux, N., et al. (2015). The EarthCARE satellite: The next step forward in global measurements of clouds aerosols precipitation and radiation. *Bulletin of the American Meteorological Society*, *96*(8), 1311–1332. https://doi.org/10.1175/BAMS-D-12-00227.1

Just, D., Gutiérrez, R., Roveda, F., & Steenbergenm T. (2014). Meteosat third generation imager: Simulation of the flexible combined imager instrument chain. Proc. SPIE 9241, sensors, systems, and next-generation satellites XVIII, 92410E (7 October 2014). https://doi.org/10.1117/12.2066872

Kay, J. E., Medeiros, B., Hwang, Y.-T., Gettelman, A., Perket, J., & Flanner, M. G. (2014). Processes controlling Southern Ocean shortwave climate feedbacks in CESM. *Geophysical Research Letters*, *41*, 616–622. https://doi.org/10.1002/2013GL058315

Kay, J. E., Wall, C., Yettella, V., Medeiros, B., Hannay, C., Caldwell, P., & Bitz, C. (2016). Global climate impacts of fixing the Southern Ocean shortwave radiation bias in the Community Earth System Model. *Journal of Climate*, *29*(12), 4617–4636. https://doi.org/10.1175/JCLI-D-15-0358.1

Komurcu, M., Storelvmo, T., Tan, I., Lohmann, U., Yun, Y., Penner, J. E., et al. (2014). Intercomparison of the cloud water phase among global climate models. *Journal of Geophysical Research: Atmospheres*, *119*, 3372–3400. https://doi.org/10.1002/2013JD021119

Lawson, R. P., & Gettelman, A. (2014). Impact of Antarctic mixed-phase clouds on climate. *Proceedings of the National Academy of Sciences of the United States of America*, *111*(51), 18,156–18,161. https://doi.org/10.1073/pnas.1418197111

Lee, T. F., Nelson, C. S., Dills, P., Riishojgaard, L. P., Jones, A., Li, L., et al. (2010). NPOESS: Next-generation operational global Earth observations. *Bulletin of the American Meteorological Society*, *91*(6), 727–740. https://doi.org/10.1175/2009BAMS2953.1

Lee, T. F., Turk, F. J., & Richardson, K. (1997). Stratus and fog products using GOES-8–9 3.9-μm data. *Weather Forecasting*, *12*, 664–677.

Li, Z.-X., & Le Treut, H. (1992). Cloud-radiation feedbacks in a general circulation model and their dependence on cloud modeling assumptions. *Climate Dynamics*, *7*(3), 133–139. https://doi.org/10.1007/BF00211155

Liou, K. N. (2002). *An introduction to atmospheric radiation*, *Int. Geophys. Ser.* (Vol. 84). San Diego, CA: Academic Press.

Mace, G. G., & Avey, S. (2017). Seasonal variability of warm boundary layer cloud and precipitation properties in the Southern Ocean as diagnosed from A-Train data. *Journal of Geophysical Research: Atmospheres*, *122*, 1015–1032. https://doi.org/10.1002/2016JD025348

Mace, G. G., Marchand, R., & Stephens, G. L. (2007). Global hydrometeor occurrence as observed by CloudSat; initial observations from summer 2006. *Geophysical Research Letters*, *34*, L09808. https://doi.org/10.1029/2006GL029017

Mace, G. G., & Protat, A. (2018a). Clouds over the Southern Ocean as observed from the RV Investigator during CAPRICORN. Part 1: Cloud occurrence and phase partitioning. *Journal of Applied Meteorology and Climatology*, *57*. https://doi.org/10.1175/JAMC-D-17-0194.1

Mace, G. G., & Protat, A. (2018b). Clouds over the Southern Ocean as observed from the RV Investigator during CAPRICORN. Part 2: The properties of non-precipitating stratocumulus. *Journal of Applied Meteorology and Climatology*, *57*. https://doi.org/10.1175/JAMC-D-17-0195.1

Mace, G. G., & Zhang, Q. (2014). The CloudSat radar-lidar geometrical profile product (RL-GeoProf): Updates, improvements, and selected results. *Journal of Geophysical Research: Atmospheres*, *119*, 9441–9462. https://doi.org/10.1002/2013JD021374

Mace, G. G., Zhang, Q., Vaughan, M., Marchand, R., Stephens, G., Trepte, C., & Winker, D. (2009). A description of hydrometeor layer occurrence statistics derived from the first year of merged CloudSat and CALIPSO data. *Journal of Geophysical Research*, *114*, D00A26. https://doi.org/10.1029/2007JD009755

Marchand, R., Mace, G. G., Ackerman, T., & Stephens, G. (2008). Hydrometeor detection using CloudSat—An Earth-orbiting 94-GHz cloud radar. *Journal of Atmospheric and Oceanic Technology*, *25*(4), 519–533. https://doi.org/10.1175/2007JTECHA1006.1

McCoy, D. T., Hartmann, D. L., & Grosvenor, D. P. (2014a). Observed Southern Ocean cloud properties and shortwave reflection. Part I: Calculation of SW flux from observed cloud properties. *Journal of Climate*, *27*(23), 8836–8857. https://doi.org/10.1175/JCLI-D-14-00287.1

McCoy, D. T., Hartmann, D. L., & Grosvenor, D. P. (2014b). Observed Southern Ocean cloud properties and shortwave reflection. Part II: Phase changes and low cloud feedback. *Journal of Climate*, *27*(23), 8858–8868. https://doi.org/10.1175/JCLI-D-14-00288.1

McCoy, D. T., Hartmann, D. L., Zelinka, M. D., Ceppi, P., & Grosvenor, D. P. (2015). Mixed-phase cloud physics and Southern Ocean cloud feedback in climate models. *Journal of Geophysical Research: Atmospheres*, *120*, 9539–9554. https://doi.org/10.1002/2015JD023603

McCoy, D. T., Tan, I., Hartmann, D. L., Zelinka, M. D., & Storelvmo, T. (2016). On the relationships among cloud cover, mixed-phase partitioning, and planetary albedo in GCMs. *Journal of Advances in Modeling Earth Systems*, *8*, 650–668. https://doi.org/10.1002/2015MS000589

Meyers, M. P., DeMott, P. J., & Cotton, W. R. (1992). New primary ice-nucleation parameterizations in an explicit cloud model. *Journal of Applied Meteorology*, *31*(7), 708–721. https://doi.org/10.1175/1520-0450(1992)031<0708:NPINPI>2.0.CO;2

Miller, S. D., Noh, Y. J., & Heidinger, A. K. (2014). Liquid-top mixed-phase cloud detection from shortwave-infrared satellite radiometer observations: A physical basis. *Journal of Geophysical Research: Atmospheres*, *119*, 8245–8267. https://doi.org/10.1002/2013JD021262

Morrison, A. E., Siems, S. T., & Manton, M. J. (2011). A three-year climatology of cloud-top phase over the Southern Ocean and North Pacific. *Journal of Climate*, *24*(9), 2405–2418. https://doi.org/10.1175/2010JCLI3842.1

Morrison, H., de Boer, G., Feingold, G., Harrington, J., Shupe, M. D., & Sulia, K. (2012). Resilience of persistent Arctic mixed-phase clouds. *Nature Geoscience*, *5*(1), 11–17. https://doi.org/10.1038/ngeo1332

Nasiri, S. L., & Kahn, B. H. (2008). Limitations of bispectral infrared cloud phase determination and potential for improvement. *Journal of Applied Meteorology and Climatology*, *47*(11), 2895–2910. https://doi.org/10.1175/2008JAMC1879.1

Naud, C. M., Booth, J. F., & Del Genio, A. D. (2014). Evaluation of ERA-Interim and MERRA cloudiness in the Southern Ocean. *Journal of Climate*, *27*(5), 2109–2124. https://doi.org/10.1175/JCLI-D-13-00432.1

Nayak, M., Witkowski, M., Vane, D., Livermore, T., & Rokey, M. (2012). CloudSat anomaly recovery and operational lessons learned. Proc. 12th Int. Conf. on Space Operations, Stockholm, Sweden, CNES, Paper 1295798. Retrieved from www.spaceops2012.org/proceedings/documents/id1295798-Paper-001.pdf

Niu, J., Carey, L. D., Yang, P., & Vonder Haar, T. H. (2008). Optical properties of a vertically inhomogeneous mid-latitude mid-level mixed-phase altocumulus in the infrared. *Atmospheric Research*, *88*(3-4), 234–242. https://doi.org/10.1016/j.atmosres.2007.11.020

Noh, Y. J., Seaman, C. J., Vonder Haar, T. H., Hudak, D. R., & Rodriguez, P. (2011). Comparisons and analyses of wintertime mixed-phase clouds using satellite and aircraft observations. *Journal of Geophysical Research*, *116*, D18207. https://doi.org/10.1029/2010JD015420

Noh, Y. J., Seaman, C. J., Vonder Haar, T. H., & Liu, G. (2013). In situ aircraft measurements of water content profiles in various midla-titude mixed-phase clouds. *Journal of Applied Meteorology and Climatology*, *52*(1), 269–279. https://doi.org/10.1175/JAMC-D-11-0202.1

Pavolonis, M. J. (2010). Advances in extracting cloud composition information from spaceborne infrared radiances: A robust alternative to brightness temperatures. Part I: Theory. *Journal of Applied Meteorology and Climatology*, *49*(9), 1992–2012. https://doi.org/10.1175/2010JAMC2433.1

Pavolonis, M. J., Heidinger, A. K., & Uttal, T. (2005). Daytime global cloud typing from AVHRR and VIIRS: Algorithm description, validation, and comparisons. *Journal of Applied Meteorology*, *44*(6), 804–826. https://doi.org/10.1175/JAM2236.1

Platnick, S., King, M. D., Ackerman, S. A., Menzel, W. P., Baum, B. A., Riedi, J. C., & Frey, R. A. (2003). The MODIS cloud products: Algorithms and examples from Terra. *IEEE Transactions on Geoscience and Remote Sensing*, *41*(2), 459–473. https://doi.org/10.1109/TGRS.2002.808301

Protat, A., Schulz, E., Rikus, L., Sun, Z., & Xiao, Y. (2017). Shipborne observations of the radiative effect of Southern Ocean clouds. *Journal of Geophysical Research: Atmospheres*, *122*, 318–328. https://doi.org/10.1002/2016JD026061

Protat, A., Young, S. A., McFarlane, S., L'Ecuyer, T., Mace, G. G., Comstock, J., et al. (2014). Reconciling ground-based and space-based estimates of the frequency of occurrence and radiative effect of clouds around Darwin, Australia. *Journal of Applied Meteorology and Climatology*, *53*(2), 456–478. https://doi.org/10.1175/JAMC-D-13-072.1

Protat, A., Young, S. A., Rikus, L., & Whimpey, M. (2014). Evaluation of the hydrometeor frequency of occurrence in a limited-area numerical weather prediction system using near real-time CloudSat-CALIPSO observations. *Quarterly Journal of the Royal Meteorological Society*, *140*(685), 2430–2443. https://doi.org/10.1002/qj.2308

Ricchiazzi, P., Yang, S., Gautier, C., & Sowle, D. (1998). SBDART: A research and teaching software tool for plane parallel radiative transfer in the Earth's atmosphere. *Bulletin of the American Meteorological Society*, *79*(10), 2101–2114. https://doi.org/10.1175/1520-0477(1998)079<2101:SARATS>2.0.CO;2

Schmit, T. J., Griffith, P., Gunshor, M. M., Daniels, J. M., Goodman, S. J., & Lebair, W. J. (2017). A closer look at the ABI on the GOES-R series. *Bulletin of the American Meteorological Society*, *98*(4), 681–698. https://doi.org/10.1175/BAMS-D-15-00230.1

Senior, C. A., & Mitchell, J. F. B. (1993). Carbon dioxide and climate: The impact of cloud parameterization. *Journal of Climate*, *6*(3), 393–418. https://doi.org/10.1175/1520-0442(1993)006<0393:CDACTI>2.0.CO;2

Shupe, M. D., Daniel, J. S., de Boer, G., Eloranta, E. W., Kollias, P., Long, C. N., et al. (2008). A focus on mixed-phase clouds: The status of ground-based observational methods. *Bulletin of the American Meteorological Society*, *89*(10), 1549–1562. https://doi.org/10.1175/2008BAMS2378.1

Shupe, M. D., Matrosov, S. Y., & Uttal, T. (2006). Arctic mixed-phase cloud properties derived from surface-based sensors at SHEBA. *Journal of the Atmospheric Sciences*, *63*(2), 697–711. https://doi.org/10.1175/JAS3659.1

Stephens, G., Winker, D., Pelon, J., Trepte, C., Vane, D., Yuhas, C., et al. (2018). CloudSat and CALIPSO within the A-train: Ten years of actively observing the earth system. *Bulletin of the American Meteorological Society*, *99*(3), 569–581. https://doi.org/10.1175/BAMS-D-16-0324.1

Stephens, G. L., Li, J., Wild, M., Clayson, C. A., Loeb, N., Kato, S., et al. (2012). An update on Earth's energy balance in light of the latest global observations. *Nature Geoscience*, *5*(10), 691–696. https://doi.org/10.1038/ngeo1580

Stephens, G. L., Vane, D. G., Boain, R. J., Mace, G. G., Sassen, K., Wang, Z., et al., & the CloudSat Science Team (2002). The CLOUDSAT Mission and the A-Train—A new dimension of space-based observations of clouds and precipitation. *Bulletin of the American Meteorological Society*, *83*(12), 1771–1790. https://doi.org/10.1175/BAMS-83-12-1771

Stephens, G. L., Vane, D. G., Tanelli, S., Im, E., Durden, S., Rokey, M., et al. (2008). The CloudSat mission: Performance and early science after the first year of operation. *Journal of Geophysical Research*, *113*, D00A18. https://doi.org/10.1029/2008JD009982

Strabala, K. I., Ackerman, S. A., & Menzel, W. P. (1994). Cloud properties inferred from 8-12 pm data. *Journal of Applied Meteorology*, *2*, 212–229.

Sun, Z., & Shine, K. P. (1995). Parameterization of ice cloud radiative properties and its application to the potential climatic importance of mixed phase clouds. *Journal of Climate*, *8*(7), 1874–1888. https://doi.org/10.1175/1520-0442(1995)008<1874:POICRP>2.0.CO;2

Tan, I., & Storelvmo, T. (2016). Sensitivity study on the influence of cloud microphysical parameters on mixed-phase cloud thermodynamic phase partitioning in CAM5. *Journal of the Atmospheric Sciences*, *73*(2), 709–728. https://doi.org/10.1175/JAS-D-15-0152.1

Tanelli, S., Durden, S. L., Im, E., Pak, K. S., Reinke, D. G., Partain, P., et al. (2008). CloudSat's cloud profiling radar after two years in orbit: Performance, calibration, and processing. *IEEE Transactions on Geoscience and Remote Sensing*, *46*(11), 3560–3573. https://doi.org/10.1109/TGRS.2008.2002030

Trenberth, K. E., & Fasullo, J. T. (2010). Simulation of present-day and twenty-first-century energy budgets of the southern oceans. *Journal of Climate*, *23*(2), 440–454. https://doi.org/10.1175/2009JCLI3152.1

Tsushima, Y., Emori, S., Ogura, T., Kimoto, M., Webb, M. J., Williams, K. D., et al. (2006). Importance of the mixed-phase cloud distribution in the control climate for assessing the response of clouds to carbon dioxide increase: A multi-model study. *Climate Dynamics*, *27*(2-3), 113–126. https://doi.org/10.1007/s00382-006-0127-7

Vergara-Temprado, J., Miltenberger, A. K., Furtado, K., Grosvenor, D. P., Shipway, B. J., Hill, A. A., et al. (2018). Strong control of Southern Ocean cloud reflectivity by ice-nucleating particles. *Proceedings of the National Academy of Sciences of the United States of America*, *115*(11), 2687–2692. https://doi.org/10.1073/pnas.1721627115

Vial, J., Dufresne, J. L., & Bony, S. (2013). On the interpretation of inter-model spread in CMIP5 climate sensitivity estimates. *Climate Dynamics*, *41*(11–12), 3339–3362. https://doi.org/10.1007/s00382-013-1725-9

Webb, M. J., Lambert, F., & Gregory, J. M. (2013). Origins of differences in climate sensitivity, forcing and feedback in climate models. *Climate Dynamics*, *40*(3–4), 677–707. https://doi.org/10.1007/s00382-012-1336-x

Winker, D. M., Pelon, J., Coakley, J. A. Jr., Ackerman, S. A., Charlson, R. J., Colarco, P. R., et al. (2010). The CALIPSO Mission: A global 3-D view of aerosols and clouds. *Bulletin of the American Meteorological Society*, *91*(9), 1211–1230. https://doi.org/10.1175/2010BAMS3009.1

Winker, D. M., Vaughan, M. A., Omar, A. H., Hu, Y., Powell, K. A., Liu, Z., et al. (2009). Overview of the CALIPSO Mission and CALIOP data processing algorithms. *Journal of Atmospheric and Oceanic Technology*, *26*(11), 2310–2323. https://doi.org/10.1175/2009JTECHA1281.1

Yang, J., Zhang, Z., Wei, C., Lu, F., & Guo, Q. (2017). Introducing the new generation of Chinese geostationary weather satellites–FengYun 4 (FY-4). *Bulletin of the American Meteorological Society*, *98*(8), 1637–1658. https://doi.org/10.1175/BAMS-D-16-0065.1

Yang, P., Liou, K. N., Wyser, K., & Mitchell, D. (2000). Parameterization of the scattering and absorption properties of individual ice crystals. *Journal of Geophysical Research*, *105*(D4), 4699–4718. https://doi.org/10.1029/1999JD900755

Yao, Z., Li, J., Weisz, E., Heidinger, A., & Liu, C. (2013). Evaluation of single field-of-view cloud top height retrievals from hyperspectral infrared sounder radiances with CloudSat and CALIPSO measurements. *Journal of Geophysical Research: Atmospheres*, *118*, 9182–9190. https://doi.org/10.1002/jgrd.50681

Zhang, D., Wang, Z., & Liu, D. (2010). A global view of midlevel liquid-layer topped stratiform cloud distribution and phase partition from CALIPSO and CloudSat measurements. *Journal of Geophysical Research*, *115*, D00H13. https://doi.org/10.1029/2009JD012143

Zelinka, M. D., Klein, S. A., & Hartmann, D. L. (2012). Computing and partitioning cloud feedbacks using cloud property histograms. Part II: Attribution to changes in cloud amount, altitude, and optical depth. *Journal of Climate*, *25*(11), 3736–3754. https://doi.org/10.1175/JCLI-D-11-00249.1

Zelinka, M. D., Klein, S. A., Taylor, K. E., Andrews, T., Webb, M. J., Gregory, J. M., & Forster, P. M. (2013). Contributions of different cloud types to feedbacks and rapid adjustments in CMIP5. *Journal of Climate*, *26*(14), 5007–5027. https://doi.org/10.1175/JCLI-D-12-00555.1